

Detailed Mid- and Far-Ultraviolet Model Spectra for Accretion Disks in Cataclysmic Binaries

Richard A. Wade¹

*Department of Astronomy & Astrophysics, The Pennsylvania State University,
525 Davey Laboratory, University Park, PA 16802-6305*

and

Ivan Hubeny¹

*AURA/NOAO, NASA Goddard Space Flight Center,
Code 681, Greenbelt, MD 20771*

ABSTRACT

We present a large grid of computed far- and mid-ultraviolet spectra (850 Å to 2000 Å) of the integrated light from steady-state accretion disks in luminous cataclysmic variables. The spectra are tabulated at 0.25 Å intervals with an adopted FWHM resolution of 1.0 Å, so they are suitable for use with observed spectra from a variety of modern space-borne observatories. Twenty-six different combinations of white dwarf mass M_{wd} and mass accretion rate \dot{m} are considered, and spectra are presented for six different disk inclinations i . The disk models are computed self-consistently in the plane-parallel approximation, assuming LTE and vertical hydrostatic equilibrium, by solving simultaneously the radiative transfer, hydrostatic equilibrium, and energy balance equations. Irradiation from external sources is neglected. Local spectra of disk annuli are computed taking into account line transitions from elements 1–28 (H through Ni). Limb darkening as well as Doppler broadening and blending of lines are taken into account in computing the integrated disk spectra. The radiative properties of the models are discussed, including the dependence of ultraviolet fluxes and colors on M_{wd} , \dot{m} , and i . The appearance of the disk spectra is illustrated, with regard to changes in the same three parameters. Finally, possible future improvements to the present models and spectra are discussed. The synthetic spectra are available as machine-readable ASCII files via *ftp*.

Subject headings: accretion, accretion disks — binaries: close — novae, cataclysmic variables — stars: atmospheres — ultraviolet: stars

¹wade@astro.psu.edu, hubeny@tlusty.gsfc.nasa.gov

1. INTRODUCTION

In most varieties of cataclysmic variable (CV) stars, the mass transfer between the Roche-lobe filling secondary star and the white dwarf primary star occurs via an accretion disk. It is clear from decades of observations and theoretical studies that this disk can dominate the ultraviolet and visible spectra of CVs, at least for the more luminous classes such as novalike variables and dwarf novae in outburst. Observations of CVs with the *IUE* observatory established the importance of the disk light in the mid-ultraviolet (*mid-UV*; roughly, ultraviolet wavelengths longward of H Lyman- α), and *Hubble Space Telescope* (*HST*) observations using *HSP*, *FOS*, and *GHRIS* have resulted in improved data for many key systems, with improved spectral and temporal resolution and enhanced signal-to-noise ratio. Observations with the ultraviolet spectrometers (UVS) aboard the *VOYAGER* spacecraft, with the *Hopkins Ultraviolet Telescope* (*HUT*), and with the Space Shuttle-borne *ORFEUS* experiments, have shown the same dominance of the disk in luminous CVs for the far ultraviolet (*far-UV*; from the Lyman edge to Lyman- α). The disk may remain dominant in less luminous CVs (mainly the dwarf novae in quiescence), or it may contribute significantly less than the white dwarf, especially if the disk is highly inclined to the observer's line of sight. In one class of CVs, the AM Her stars, the accretion flow is channeled by strong magnetic fields and a disk is not formed.

To make the most of the large and increasing archive of high quality mid- and far-UV observations of disk-dominated, high-luminosity CVs, and to distinguish reliably between white dwarf and disk spectra in less luminous cases, it is clearly necessary to have up-to-date models for the spectral energy distribution and detailed line spectra of disks, for a variety of accretion rates, central white dwarf masses, and viewing angles (orbital inclinations). As observations have been collected over the years, different techniques, involving different levels of approximation, have been applied to this task, and a few small grids of models have been produced. For example, Williams and Ferguson 1982 described a small grid of LTE disk models, spanning the transition from optically thin to optically thick in the continuum, in which the disk was assumed to have constant temperature in the vertical direction at each radius. Wade 1984 discussed the UV and optical continua for CV ac-

cretion disks, comparing two grids of spectra, based on blackbody energy distributions and computed stellar fluxes from the Kurucz (1979) grid. la Dous (1989) introduced some absorption lines from metals into her computed ultraviolet spectra of disks, which were LTE models based on the Eddington approximation without any attempt to ensure energy balance. la Dous also summarizes prior work by other authors (see also la Dous 1994).

Recent data obtained using the instruments listed above, with their higher S/N ratios and spectral resolution, demand more detailed models, computed with some attention given to the properties of disk spectra that may distinguish them from sums of stellar atmosphere fluxes. The spectra in Wade (1984), for example, are coarsely binned and entirely inadequate for the resolution achieved in *HUT* or *HST* spectra. Many studies of individual CVs in recent years have made use of improved detail in model spectra (e.g., Long et al. 1994; Knigge et al. 1997; Knigge et al. 1998), but there has been a lack until now of a grid of mid- and far-UV spectra of disks, presented as a body. Such a grid can enable comparisons among objects, allow the range of temperatures in the disk to be estimated, help identify lines and blends that can distinguish disk spectra from white dwarf spectra, and perhaps in favorable cases help determine the mass accretion rate and orbital inclination in some CVs.

It is also desirable to have a new grid that explicitly tabulates spectra for disks viewed at a variety of inclinations, since it is clear that limb darkening of the UV light from a disk is of comparable importance to purely geometric effects for optically thick disks viewed at high inclination (e.g. Diaz, Wade, & Hubeny 1996; Wade 1996; Robinson et al. 1995; Robinson, Wood, & Wade 1998). This was shown in the early calculations of Herter et al. (1979), and has been illustrated from time to time (e.g., la Dous 1989), but most discussions of disk spectra since then have treated angle-averaged quantities. Diaz et al. (1996) discussed several aspects of limb darkening for a grid of 14 model disks, but tabulated limb-darkened fluxes at only one wavelength.

In this contribution, we present model mid- and far-UV spectra for accretion disks in CVs, for a range of white dwarf mass M_{wd} , mass transfer rate \dot{m} , and inclination angle i , that covers the expected range of interest for luminous (or "high-state") accretion disk systems. These models treat steady-state accretion disks in vertical hydrostatic equilibrium, with the en-

ergy balance of the disk computed in a self-consistent way. The modeling assumptions and techniques are described in Sections 2 and 3. Properties of the model disks and especially their spectra are the subject of Section 4. Such grids of model disk spectra need not be perfect to be useful, especially when used in a comparative way, or as a starting point in examining which way models should be improved or extended. We discuss some of these issues briefly in Section 5.

The spectra discussed here are available in tabular form as ASCII files via *anonymous ftp* (see Section 3).

2. MODEL ASSUMPTIONS AND CHOICE OF GRID

2.1. Steady-State Disk Model Computations

Our grid of spectra is constructed as follows. The disk is assumed to be axisymmetric and geometrically thin. The disk is assumed to be in steady state, that is the mass transfer rate \dot{m} is assumed to be the same at all radii. Each elementary area of the visible disk surface is assumed to make a contribution to the integrated spectrum of the disk, according to its projected surface area and at a projected Doppler shift, computed assuming circular Kepler orbits around a central white dwarf star of mass M_{wd} and radius R_{wd} .

The effective temperature, which describes the total radiation energy flux at the disk surface, is given by (see, e.g., Pringle 1981)

$$T_{\text{eff}}(r) = T_* x^{-3/4} (1 - x^{-1/2})^{1/4}$$

where $x = r/R_{\text{wd}}$, and

$$\sigma T_*^4 \equiv \frac{3GM_{\text{wd}}\dot{m}}{8\pi R_{\text{wd}}^3}$$

or

$$T_* = 64800 \text{ K} \left[\left(\frac{M_{\text{wd}}}{1 M_{\odot}} \right) \left(\frac{\dot{m}}{10^{-9} M_{\odot} \text{ yr}^{-1}} \right) \left(\frac{R_{\text{wd}}}{10^9 \text{ cm}} \right)^{-3} \right]^{1/4}$$

The maximum effective temperature $T_{\text{max}} = 0.488T_*$ occurs at $x = 1.36$.

The construction of a disk spectrum proceeds in four stages. First, the disk is divided into a set of concentric rings or annuli, with each annulus behaving as an independent plane-parallel radiating slab. The vertical structure of each ring is computed, using the program TLUSDISK (Hubeny 1990a, b), which

is a derivative of the stellar atmosphere program TLUSTY (Hubeny 1988). The computation treats the entire vertical structure of each ring, from the midplane to the surface, without any artificial introduction of the notion of a distinct “disk atmosphere”. The disk stratification is computed in the LTE approximation. Hydrostatic equilibrium is assumed, with a height-varying (tidal) gravitational acceleration. Energy balance is enforced between radiative losses at the disk surface and heat generation due to viscosity, the latter distributed throughout the vertical extent of the disk. It is assumed that there is no flux incident on the disk surface from outside.

In the specific calculations presented in this paper, the number of depths between disk mid-plane and disk surface is 99. The viscosity prescription is based on a Reynolds number approach (Lynden-Bell & Pringle 1974; Kříž & Hubeny 1986). A value of $Re = 5000$ is assumed for all radii. A parameter ζ introduced by Kříž & Hubeny (1986) controls the vertical distribution of viscous heat input. In the present work, $\zeta = 2/3$. The contribution of microturbulence to the gas pressure is assumed to be zero in the present work.

Second, the spectrum synthesis program SYN-SPEC described by Hubeny, Lanz, & Jeffery (1994) is used to solve the radiative transfer equation to compute the local, rest-frame spectrum for each ring of the disk. In addition to detailed profiles of the H and He lines, the spectrum synthesis includes “metal” lines up to $Z = 28$ (Ni), dynamically selected from the extensive line list of Kurucz & Bell (1995; see also Kurucz 1991). Typically, many thousands of lines are included in the rest-frame spectrum of each ring. At this stage, the wavelength array is irregular and differs for each ring. In addition to the angle-averaged Eddington flux $H(\lambda)$, specific intensities $I(\lambda; \mu)$ at a number of emergent angles i are computed and stored in this step.

Third, the rest-frame intensities are combined to generate an integrated disk spectrum, using the program DISKSYN5a as described more fully in §3. Fourth, the monochromatic fluxes f_{λ} are convolved with an adopted Gaussian instrumental broadening function and resampled uniformly in wavelength.

2.2. Choice of Grid Parameters

In our framework, a steady-state disk model is specified by choice of the parameters M_{wd} , R_{wd} , \dot{m} ,

Re , and ζ . These are supplemented by data that determine the details of how the programs TLUSDISK and SYNSPEC compute the atmosphere and spectra. This section describes the selection of the main parameters of the grid.

Disk models have been computed on a grid of M_{wd} and \dot{m} with almost-regular spacing but irregular grid boundaries. The choice of M_{wd} is assumed to specify R_{wd} through the mass-radius relation for cold electron-degenerate matter. We use an analytical mass-radius relation from P. P. Eggleton (private communication; cf. Nauenberg 1972). Table 1 lists for each choice of M_{wd} the corresponding white dwarf radius R_{wd} , surface gravity $\log g$ (in cgs units), Keplerian orbital speed at the surface v_{surf} , and the combination $M_{\text{wd}}/R_{\text{wd}}^3$ which enters into the formula for T_* given above. The values of \dot{m} were chosen to increase by factors of $\sqrt{10} \approx 3.16$, and the intent was to have $M_{\text{wd}}/R_{\text{wd}}^3$ increase by the same ratio from one choice of M_{wd} to the next, so that the same T_* would apply to several different combinations of M_{wd} and \dot{m} in the grid; this was achieved for all except the last step in M_{wd} , where the factor is only 3.01.

The original grid extended only to $\dot{m} \leq 10^{-9} M_{\odot} \text{ yr}^{-1}$, but was later extended. Thus the labeling of models by letters, shown in Table 2, is slightly irregular. This table gives for each disk model: the white dwarf mass M_{wd} , the mass transfer rate \dot{m} , the number of annuli computed, the maximum effective temperature of the disk (occurring at $x = r/R_{\text{wd}} = 1.36$), the Rosseland optical depth τ_c to the disk midplane at that disk radius, the effective temperature and optical depth for the outermost (last) ring, and the radius of the disk.

For each disk model, stratified atmospheres and spectra were computed at a set of radii that increase approximately logarithmically from the innermost radius, which is always $x = R_{\text{min}}/R_{\text{wd}} = 1.05$. The spacing of rings was chosen to ensure a sufficiently dense sampling of $T_{\text{eff}}(r)$. The outermost ring was chosen so that $T_{\text{eff}}(R_{\text{out}})$ would be near 10,000 K, since cooler zones at larger radii contribute in only a minor way to the far- and mid-UV disk flux. (This point is discussed further in §4.4 below.) Table 3 gives the radii and effective temperature structure for a number of representative models. For other models the dimensionless radii x are the same. The temperature structure of other models can be estimated closely from the tabulated model that has nearly the same T_{eff} at $x = 1.36$ (see Table 2, or calculated directly from the formulas given above).

The operation of program TLUSDISK is controlled by a data file that, among other things, specifies the details of opacity and equation of state calculations. In our models H and He always contributed to the equation of state; in some models cooler than 12,000 K, the first 30 elements of the periodic table were used. Hydrogen bound-free continua arising from the eight lowest energy levels were always included in the opacity calculation. Continua from fourteen levels of He I were included for models hotter than 12,000 K, and eight levels of He II were also included for models hotter than 25,000 K. Other opacity sources included electron scattering and free-free continua, and the H^- bound-free and free-free continua when applicable. For models cooler than 16,000 K, the atmosphere computation was carried out with 53 frequency points defining the continuum; for models between 16,000 K and 30,000 K, 59 frequency points were used; for models with $T_{\text{eff}} > 30,000$ K, 65 frequency points were employed.

For each ring of each disk model, the atmosphere calculation was started with a gray LTE disk model (Hubeny 1990a) in hydrostatic equilibrium, then iterated to thermal equilibrium. The convergence criterion was that the last relative change in any model quantity be smaller than 10^{-3} .

3. SPECTRUM SYNTHESIS FOR RINGS AND DISKS

The radiative transfer solution to compute the detailed emergent spectrum from each ring was done by SYNSPEC at essentially full resolution. That is, the maximum spacing between adjacent wavelengths, which is 0.01 Å for $\lambda < 1300$ Å and 0.02 Å for $\lambda > 1300$ Å, is nearly small enough to resolve the thermal Doppler width of metal lines. Microturbulent broadening of lines was assumed to be zero. The spacing of computed wavelengths in SYNSPEC is done to ensure that there is a wavelength point at the center of each line that contributes to the spectrum, and at least one wavelength point between each adjacent pair of lines. Thus the wavelength grid is irregular at this stage of computation.

For each ring, both angle-averaged fluxes H_{ν} and specific intensities I_{ν} are computed. The I_{ν} computation is done for $\mu \equiv \cos i = 1.00, 0.75, 0.50$, and 0.25. I_{ν} is converted to I_{λ} in subsequent computational steps.

To compute the integrated disk spectrum, a sum-

mation over rings is carried out. Each ring is divided into a large number of azimuthal sectors, and the contributions are summed with appropriate area weighting and Doppler shifting. The size of the Doppler shift (due to projected orbital motion of the gas) and the specific intensity both vary depending on the inclination i of the disk symmetry axis to the line of sight. For arbitrary values of $\mu = \cos i$, the intensity $I_\lambda(\lambda; \mu)$ is interpolated linearly in μ between the pre-computed $I_\lambda(\lambda; \mu)$. Here $I_\lambda(\lambda; \mu = 0)$ is assumed to be zero.

The resulting disk spectrum is sampled rather finely, with a uniform sampling interval of 0.05 Å. Since the orbital Doppler motions of the gas in the disk have smeared each line substantially for all but exactly face-on orientations, this high sampling frequency is redundant. The spectra are convolved with an instrumental profile and sampled with four wavelength points per FWHM. Except when resolution is specifically discussed, all of the spectra described here or available as machine-readable files have been convolved with a Gaussian profile whose FWHM is 1.0 Å.

Disk spectra have been computed and tabulated for six inclination angles i . Table 4 provides a handy correspondence between μ , i , and $\sin i$, which is the factor by which orbital motions in the disk are projected on the line of sight. The six angles are sufficient to show the dependence of the observed spectrum on the inclination, but may not always be sufficient to allow direct interpolation for the purposes of detailed fits of data. Denser sampling of i or computation of synthetic spectra for specific “off-grid” angles is straightforward; interested readers may contact the first author.

The disk spectra are presented for a “*non-projected*” disk viewed from a distance of $d = 100$ pc. The calculation thus amounts to approximating the flux integral

$$f_\lambda(\lambda; \mu) = \frac{1}{d^2} \int_{R_{\min}}^{R_{\max}} dr \int_0^{2\pi} r d\phi \\ \times \int_0^\infty d\lambda' I_\lambda(\lambda', r, \mu) V(r, \phi, \mu) \Delta$$

where

$$\Delta \equiv \delta \left(\lambda - \lambda' \left[1 + \frac{1}{c} \left(\frac{GM_{\text{wd}}}{r} \right)^{1/2} \sin i \sin \phi \right] \right).$$

Here δ is the Dirac delta-function, so that the Doppler-shifting function Δ selects the appropriate

rest-frame wavelength λ' that contributes at the observer’s wavelength λ . Therefore the spectra do correctly take account of projected *velocities*.

The visibility factor $V(r, \phi, \mu)$ in the formula makes allowance for the presence of an opaque central body (the white dwarf) that occults a portion of the inner disk. That is, some of the innermost sectors do not contribute to the integrated disk spectrum, if they would be blocked from view by the white dwarf. This visibility factor is not the same as the visibility factor for a “flared” disk, as discussed by Robinson et al. (1995) or Robinson, Wood, & Wade (1998). In the present work flaring effects are neglected (but see the discussion in §4.1).

It is important to note that the results illustrated in this paper, as well as the tabulated spectra, *do not* include a factor $\cos i$ representing the geometric foreshortening of the (flat) disk, that would normally appear as a multiplicative factor in the expression above. This factor is omitted, so that the full effect of limb darkening alone can be judged from the figures.

To be compared with actual data, the present synthetic disk spectra must be supplemented with a model spectrum of the central object, itself with a suitably disk-occulted lower hemisphere. This white dwarf spectrum is omitted from the results shown here. The size of the white dwarf’s contribution to the total system light is discussed briefly in §4.3. Nguyen et al. (1998) have presented some examples of synthetic solar-abundance white dwarf spectra for the mid-UV. A large grid of theoretical solar-composition white dwarf model atmospheres has been constructed, and will be published in due time (Hubeny & Lanz, in prep.). The interested reader may contact I.H. for more information and selected models.

ASCII tables of the synthetic disk spectra are available in machine-readable form by *anonymous ftp* from `ftp.astro.psu.edu` in directory `pub/wade/disks`. There are 26 different files, each corresponding to one disk model (as listed in Table 2). Each file contains a single header line, followed by 4601 data lines. Each data line contains seven columns: wavelength followed by non-projected flux f_λ in $\text{erg cm}^{-2} \text{s}^{-1} \text{Å}^{-1}$ for six values of μ . The initial and final wavelengths are 850.00 Å and 2000.00 Å, and the wavelength spacing is 0.250 Å. Table 5 shows excerpts from the file `zz.grid` for disk model `zz`. Publications making use of these tables should make bibliographic citation of the present paper.

4. SOME PROPERTIES OF THE RING AND DISK SPECTRA

4.1. Disk Vertical Structure

A detailed discussion of the stratification of disk models is left to another paper. A couple of issues deserve mention, since they relate to the reliability of the approximations made in computing the present spectra.

All the rings in all the models have Rosseland optical depths $\tau_c \gtrsim 1$, where τ_c is measured vertically, from the outside of the disk to the disk midplane. (Note that the Rosseland depth referred to is computed using only the continuous opacity sources.) This high optical depth helps to ensure that: (1) the local photosphere, defined as a geometrical region where most of the observed spectrum features originate, i.e., where the monochromatic optical depths measured from the surface are of the order of unity, is a relatively thin layer on top of the bulk of the disk, consistent with the plane-parallel approximation; (2) the local atmosphere can be considered as being laterally homogeneous, also consistent with the plane-parallel assumption; and (3) the formation of (weak) absorption lines is not unduly affected by shear due to differential rotation of the disk, consistent with the hydrostatic approximation. In disk models with lower values of \dot{m} than considered here, some rings may become optically thin in the continuum, so that the thermal balance of the bulk of the disk is dominated by line cooling. In that case, the details of radiative transfer in the lines, such as turbulent or shear broadening, become overwhelmingly important, and the strong lines are in emission. In the present models, it is expected that such effects are at least not dominant for the computed absorption spectrum. The lowest values of the midplane optical depth are attained in the inner disk, inside the maximum of T_{eff} . They are lowest for models with the lowest \dot{m} at a fixed M_{wd} , or for the highest M_{wd} at a fixed \dot{m} , reaching $\tau_c \approx 1$ for $\dot{m} = 10^{-10.5} M_{\odot} \text{ yr}^{-1}$ and $M_{\text{wd}} = 1.210 M_{\odot}$ (model x) at $x = 1.05$.

The assumption that the photosphere of the disk is planar was made in combining the ring spectra to make the integrated disk spectra. As will be discussed elsewhere, the opening angles of the disk are typically $\theta \sim h/r < 0.1$ radian. For the most extreme inclinations discussed here, differential visibility of the “front” and “back” halves of the disk, combined with a non-negligible difference in limb darkening of the

front and back halves, should be taken into account (see, e.g., Robinson et al. 1995; Wade 1996; Robinson, Wood, & Wade 1988). However, this is most important in considering situations in which the disk is effectively resolved, such as by eclipse mapping, rather than for the integrated light of disks. Another caution is that the present models do not include any radiation from an outer disk “rim”.

4.2. Properties of Spectra of Individual Rings

Because the disk atmospheres considered here are optically thick, there is a fairly close resemblance between the emitted rest-frame spectrum from some disk annulus and the spectrum from a (plane-parallel) stellar atmosphere, having the same T_{eff} and with $\log g$ corresponding to the effective gravity at the photosphere of the disk. Small details will be different, since hydrostatic equilibrium is solved in one case under conditions of constant gravitational acceleration, and in the other case with a gravitational acceleration that increases approximately linearly with distance from the midplane. Another potential difference between the disk and atmospheric structure arises because the total flux is constant with depth in the case of stellar atmospheres, but departs from constancy in disks. On the other hand, both stellar and disk atmosphere models solved in LTE have similar temperature stratification: in both cases the local temperature monotonically decreases outward, so major features of the spectrum, such as absorption line formation and limb darkening, are shared in common.

(To be more general, the local temperature decreases vertically in disks, only when the viscosity power-law exponent ζ is chosen to be larger than about 0.5 for typical cases. For lower values, i.e., when the kinematic viscosity does not decrease sufficiently rapidly towards the disk surface, one faces the so-called disk thermal catastrophe [e.g. Shaviv & Wehrse 1986]. This is a sharp increase of local temperature in the superficial layers, where energy is still generated by viscous dissipation, while all radiative cooling transitions are optically thin and therefore ineffective in carrying away the generated energy. With our choice of ζ this catastrophe does not occur.)

Figure 1 illustrates the computed rest-frame spectra of three rings (18, 22, 26) from model jj , for the region 1500 – 1600 Å. The effective temperatures of these rings are 29150 K, 19650 K, and 13140 K. Angle-averaged Eddington fluxes, $\log H_{\lambda}$, are shown. The left panel (a) shows the spectra at the full computed

resolution, while the right panel (b) shows the same spectra convolved with a Gaussian instrumental profile (FWHM = 0.2 Å, corresponding to 39 km s⁻¹) and sampled every 0.05 Å. Even with this very modest instrumental broadening, it is clear that information is lost. In a disk spectrum, however, the situation is even worse: the Keplerian speed of these rings would be ~ 1565, 1180, and 890 km s⁻¹, respectively, so the blending of lines due to a mixture of projection factors $v(r) \sin i \sin \phi$ is quite severe, even at low inclination. For this reason the disk spectra discussed below are convolved with a wider Gaussian (FWHM = 1.0 Å) without significant loss from the point of view of comparison with observation. Blending is discussed further, below.

Figure 1 also illustrates the dependence of certain spectral features on effective temperature. Notable are the Si II lines near 1530 Å, the C IV doublet at 1550 Å, and the group of lines near 1560 Å (mainly C I, Si I, and Fe II), each of which forms at a characteristic range of temperatures. In a disk spectrum, each of these spectroscopic features will be kinematically broadened by an amount characteristic of its radius in the disk. The integrated disk spectrum thus encodes, in a complicated way, the $T_{\text{eff}}(r)$ structure of the disk. Decoding this scrambled message necessarily requires spectrum synthesis of the kind presented here.

4.3. Properties of Integrated Disk Spectra

Figure 2 shows the far-UV spectrum of a nearly face-on disk, model *bb*, viewed at inclination $i = 8^\circ:1$ ($\mu = 0.990$), for three different instrumental resolutions (Gaussian FWHM = 0.1, 1.0, and 3.5 Å). The smallest FWHM corresponds to a resolution slightly worse than that of the *ORFEUS* Berkeley spectrometer or the *FUSE* spectrometers, while the largest FWHM corresponds to the *HUT* spectrometer. For this extreme case of minimal Doppler broadening and blending of lines, it is clear that improving the FWHM from 3.5 Å to 1.0 Å results in an increase of usable information, while further improving the FWHM to 0.1 Å does not result in significant new information about line formation in the disk. Indeed the difference between the 0.1 Å and the 1.0 Å cases is barely noticeable at the scale of the figure, in the cores of the lines. This shows again that the adopted FWHM = 1.0 Å is a reasonable choice.

At a fixed distance from the observer, a disk can appear brighter if it is made hotter at constant size

(higher T_{max} from higher \dot{m}), if it is made larger while keeping T_{max} the same (lower M_{wd} , hence larger R_{wd} , requiring an increase in \dot{m}), or if it is tilted closer to a face-on orientation (increased projected area, and diminished limb darkening). A disk will generally appear “bluer” (relatively more flux at shorter wavelengths) if T_{max} is higher, or if μ is larger (limb darkening is stronger at shorter wavelengths). If T_{max} and μ are kept constant along a disk model sequence of changing M_{wd} (such as the sequence *x*, *t*, *p*, *k*, *aa*), the effects on the spectrum are expected to be more subtle, due to different effective gravities and different orbital speeds (hence different line blending) for corresponding rings in different models. Some of these effects are illustrated below, while others are better studied with the aid of the machine-readable files.

Figure 3 shows, for a fixed viewing angle $\mu = 0.75$, how the flux at 1455 Å varies with changes in the mass transfer rate, along sequences of constant white dwarf mass and radius, and along sequences of constant T_{max} (recall $T_{\text{max}} = T_{\text{eff}}$ at $x = 1.36$). At constant M_{wd} , increasing \dot{m} raises the effective temperature of each disk ring, and also raises the fluxes from the disk as a whole. At fixed T_{max} , *decreasing* M_{wd} increases the flux from the disk, since the scaling of temperature with dimensionless radius x is not changed, but the linear scale of the disk increases with R_{wd} .

It was noted earlier that the model spectra presented here do not include the white dwarf’s contribution to the light (but do account for occultation of the inner disk by the white dwarf). As a rough guide for comparing the white dwarf flux with the disk fluxes shown in Figure 3, an (unocculted) white dwarf of radius 10⁹ cm, viewed from a distance $d = 100$ pc, produces a flux at 1455 Å of $\log f_\nu \approx 0.5, 0.8, 1.0, 1.1,$ and 1.2 (mJy) for effective temperatures of 25000, 30000, 35000, 40000, and 45000 K, respectively. Fluxes for other white dwarf radii can be derived by appropriate scaling. For an opaque disk with $R_{\text{min}} = R_{\text{wd}}$, the projected geometrical area of the white dwarf is reduced by a factor $(1 + \cos i)/2$ owing to occultation by the disk. The white dwarf may be competitive with the disk in the mid-UV, provided it is sufficiently hot, and either M_{wd} or \dot{M} is sufficiently small, or if the disk is viewed at a high inclination angle.

Figure 4 shows, also for $\mu = 0.750$, the behavior of two disk flux ratios, $f_\nu(1075 \text{ Å})/f_\nu(1455 \text{ Å})$ and $f_\nu(1455 \text{ Å})/f_\nu(1945 \text{ Å})$, as \dot{m} is varied. The former ratio relates far-UV and mid-UV flux, while the latter

ratio is a measure of the mid-UV slope of the spectrum. As before, solid lines connect models at the same M_{wd} , while dashed lines connect models having the same T_{max} . At T_{max} increases, the flux ratios (or colors) become “bluer”. The mid-UV slope is relatively insensitive to disk properties, and above $T_{\text{max}} \sim 39,000$ K shows hardly any change. The far-UV/mid-UV ratio is more sensitive to T_{max} , as expected. Note that the flux ratios are sensitive to disk inclination, through the effect of limb darkening, discussed below.

The previous two figures illustrated the behavior of disk fluxes for a fixed viewing direction, $\mu = 0.75$. Even apart from effects resulting from the changing projected area, the flux from a disk will change with μ owing to limb darkening. The colors (i.e., flux ratios) will change as well, since limb darkening is wavelength dependent. These effects are illustrated in Figure 5, which shows $\log f_{\nu}$ vs μ for two disks, models *bb* and *z*, at three wavelengths 1075 Å, 1455 Å, and 1945 Å.

Limb darkening occurs for both stars and disks. Invoking the classical Eddington-Barbier relation, the specific intensity $I_{\nu}(\mu) \approx S_{\nu}(\tau_{\nu} = \mu)$, where S_{ν} is the source function, given in LTE by the Planck function, $B_{\nu}(T)$. Since the temperature decreases (vertically) outward, the specific intensities at lower values of μ sample lower-temperature regions, thereby producing a spectral energy distribution that is both redder and dimmer. In the case of disks there is no averaging over a hemisphere as there is in the case of stars, because disks lack spherical symmetry. The full effect of limb darkening is therefore observable, and disks appear very considerably dimmer and reddened when viewed at high inclination. Diaz, Wade, & Hubeny (1996) have discussed ultraviolet limb darkening for disks in detail.

Attention is now turned from photometric properties to the appearance of the actual disk spectra. Figure 6 shows a sequence of far-UV f_{λ} spectra for disks around a $M_{\text{wd}} = 0.80 M_{\odot}$ white dwarf, viewed with $\mu = 0.50$, normalized near 1330 Å. The quantity that varies is the mass transfer rate \dot{m} . The dramatic change in overall spectral slope is due to the increasing temperature of the disk. The hydrogen lines, too, show changes in strength and profile. Two effects are at work for the lines: (1) as the disk becomes hotter overall, relatively larger areas of the disk are formed at high temperatures where the H lines are weak; (2) as the disk is made hotter, the location in the disk at which the H lines attain maximum strength moves

outwards, toward lesser orbital speeds and smaller associated Doppler broadening.

The change in line shape due to the change in Doppler broadening is also noticeable in the weaker lines. For example, near 1135 Å note how “absorption” metamorphoses into “emission” at the highest \dot{m} . This is actually a case of separate features combining in the less luminous models to form a single absorption feature, placed roughly halfway between their rest wavelengths, but only if the disk is cool enough overall that these features are formed in the inner disk where orbital speeds are high. (See also Figure 8.)

Figure 7 shows the mid-UV spectra for the same sequence of disk models, again viewed at $\mu = 0.50$. The normalization of spectra is now at 1950 Å. Hotter disks are “bluer” (more flux at short wavelengths), and the detailed line spectra again show sensitivity to (1) the effective temperatures attained in the disk and (2) the velocities characterizing the radii in the disk where those temperatures are attained.

Another view of the far-UV spectrum is provided in Figure 8, where a single disk model, *bb*, is viewed from a variety of different lines of sight labeled by μ . Recall that the geometric projection factor $\cos i = \mu$ is not included, so the change in flux levels shown in the figure is due to limb darkening alone. Limb darkening is very strong in the ultraviolet, and is sensitive to both temperature and wavelength. Also evident is the strong dependence of the shape and strength of features on inclination angle. Since different μ 's correspond to different velocity projection factors, the pattern of minima and maxima in the disk integrated spectrum changes markedly from one example to the next. Individual features appear to broaden, split, merge, or shift their locations. The overall spectrum becomes smoother when the disk is viewed more nearly edge-on.

Note in Figure 8 how local maxima in the disk flux may appear at the rest wavelengths of strong features, when the feature has been split in two by the Doppler effect, such as the 1085 Å line of He II, viewed at $\mu = 0.500$. Lines formed at high temperature in the inner disk will be broadened more, at a particular inclination, than lines formed in the more slowly moving, cool outer disk. Thus a single “broadening convolution” cannot be applied to a disk spectrum, as it can be to the spectrum of a single star: spectrum synthesis is mandatory.

A final exploration of the dependence of disk spectra on temperature is provided by Figure 9, which shows the region 1300 – 1700 Å for a sequence of disks with increasing \dot{m} onto a 0.80 M_{\odot} white dwarf. The viewing angle is nearly face-on in this diagram, and fluxes are plotted logarithmically to facilitate comparison of feature strengths in one model with another. “Cooler” disks (models m , n , p) show certain absorption features more strongly than hot disks, and *vice versa*. Thus, the integrated disk spectra do retain, in some measure, information concerning the local, rest-frame spectra (cf. Figure 1) of the rings from which they are constituted. This information appears in a diluted and convoluted form, which makes interpretation of the spectra difficult. However, it is the most direct connection to the physics of a disk atmosphere.

An important question is whether the ultraviolet spectrum of a steady-state accretion disk is sufficiently distinctive to enable the white dwarf mass, mass transfer rate, and inclination to be recovered uniquely. The preceding discussion shows that in many cases it will be possible to make useful distinctions among the models. However, it is possible to find pairs of spectra that are very similar. Figure 10 compares two models, cc and v which have the same value of T_{\max} , achieved through different combinations of M_{wd} and \dot{m} . Since M_{wd} differs, there is a difference in the Keplerian orbital speed of gas in the inner disk, but different viewing angles can be chosen to match the *projected* velocities of the disk gas, about 3400 km s⁻¹ in this case. Likewise, the fluxes from the two model disks can be scaled to match at some wavelength, as if choosing the distances from which the disks are viewed. The result of this matching, as shown by the Figure, is two spectra that are nearly indistinguishable. The remaining differences are due to different amounts of “reddening” from limb darkening and a small difference in the effective photospheric gravity of the two disks. The differences are subtle and might pass unnoticed or be attributed to differences in interstellar reddening, for example. Yet the difference in \dot{m} is more than a factor of three!

Additional, rather precise, knowledge about an observed system may be required to break such a degeneracy of model spectra that match the spectroscopic observations about equally well. This information might concern the orbital inclination, the white dwarf mass, or the distance. The specific match chosen for illustration does not involve matching extreme values of mass, inclination, or distance, however, and

if encountered in practice would require precision of measurement better than is usually attained, in order to distinguish the models.

4.4. Missing Flux Due to Truncation at $T(r) \approx 10,000$ K

An important consideration in using these models is to what extent flux is missing, due to the fact that the spectrum synthesis was stopped when T_{eff} fell below roughly 10,000 K. This missing flux may on the one hand affect the overall “color” of the integrated spectra, and may on the other hand affect the details of line blending and feature strength. The expectation is that, although the outer disk (i.e., $r > R_{\text{out}}$ of the present models) is large in surface area, it is cool enough that the contribution in the far- and mid-UV spectral region can be neglected.

The missing flux question was investigated quantitatively for seven models (m , s , t , u , v , dd , jj) representing the whole range of T_{\max} of the disk model grid. From visual inspection of all the individual ring spectra of model jj , three wavelength intervals were selected, each 10 Å wide and centered at 1075 Å, 1455 Å, and 1945 Å. In these intervals, the line blocking is relatively small and either consistent or smoothly varying over the range of temperatures that was modeled. For each spectral interval and each of the seven disk models, mean fluxes H_{ν} and intensities I_{ν} were computed, ring by ring. Plots of $x^2 H_{\nu}(x)$ and $x^2 I_{\nu}(x)$ against $\ln x$ ($x = r/R_{\text{wd}}$) were constructed, and these were used to extrapolate $x^2 H_{\nu}(x)$ or $x^2 I_{\nu}(x)$ smoothly to zero in the outer disk. Numerical integrations of $H_{\text{total}} = 2\pi \int x H_{\nu}(x) dx = 2\pi \int x^2 H_{\nu}(x) d(\ln x)$ over the extrapolated disk and over the actually computed disk limits were then compared. A similar procedure was used with I_{ν} .

In this way it was estimated that at 1075 Å, an error is made that is never larger than 0.2 per cent for any disk model, either for angle-averaged flux or for specific intensity. For 1455 Å, the maximum error grows to 3.5 per cent (for the coolest overall model, model m). At 1945 Å, the maximum estimated missing flux is largest, as would be expected, amounting to 9.3 per cent for model m , but no larger than 3.1 per cent for models as hot or hotter than model u . The error in intensity is largest when the disk is viewed nearly face-on ($\mu = 1$). At large inclination angles limb darkening, which is stronger at a fixed wavelength for cooler atmospheres, diminishes the relative importance of the missing outer disk.

As a further check, angle-averaged fluxes H_λ for solar-abundance *stellar* atmospheres (Kurucz 1994) were used to synthesize approximate disk spectra corresponding to models m , s , t , u , v , dd and jj . These were truncated at $T_{\text{out}} \approx 10000$ K (as with the self-consistent disk models described here), and alternatively at $T_{\text{out}} \approx 4000$ K. Comparison of the disk fluxes gives truncation errors directly for these stellar atmosphere-based model disk spectra. These errors are very similar to the truncation errors for the self-consistently computed disk spectra of this paper, as estimated by the extrapolation method described above.

5. DISCUSSION

Modern observations of CVs in the ultraviolet are frequently of good enough quality that they deserve to be compared with model spectra that are more detailed than models used in the past. The grid of model spectra presented here is intended to provide a basis for such comparisons. The construction of the spectra involves many decisions, such as what level of approximation is to be used, or what values or ranges of parameters are to be considered, so these topics have been addressed at some length. Also, the illustrative comparison of models has been emphasized, to show the dependence of the spectrum on \dot{m} , μ , etc.

Detailed analysis of observed CV spectra is beyond the scope of this presentation, as it involves a host of additional considerations pertaining to individual objects. These may include such things as interstellar reddening and the extent to which the white dwarf mass or orbital inclination may be constrained from orbital studies. It is appropriate, however, to review briefly some issues that may arise during the comparison of model spectra and observed spectra. We emphasize that the models presented here, although advanced by comparison with past efforts, and certainly suitable for use, also represent a starting point for improved future models.

The present disk spectra do not include the contribution from the central white dwarf or its boundary layer. The boundary layer is expected to contribute mainly in the extreme ultraviolet, $\lambda < 911 \text{ \AA}$ (Wade 1991; Polidan, Mauche, & Wade 1990). The white dwarf's contribution to the far- and mid-UV spectrum can be estimated (see §4.3), and can be readily computed and included.

The present disk models and spectra are based on

vertical hydrostatic equilibrium. Observations show that among luminous CVs, many of the resonance lines and stronger subordinate lines in the UV exhibit P-Cygni or blue-shifted absorption profiles, indicating that a wind exists. Likely, this wind arises from the disk, rather than from the central star (Pereyra, Kallman, & Blondin 1997; Proga, Stone, & Drew 1998). The direct observational consequence of the wind is that several of the more obvious spectral diagnostics cannot be used, that would otherwise provide information about the properties of the disk. More subtle problems may also arise, if the weak UV lines are formed in gas that already participates in the outflow, or if the spectrum is formed in an extended zone that undermines the plane-parallel (i.e., laterally homogeneous) approximation that was used in computing the models of disk annuli. Further modeling will be required to address these questions.

The disk stratifications computed here, and the spectra derived from them, do not include the effect of irradiation by an external source, whether it is direct illumination of the disk by the central star, illumination of the outer disk by the hotter inner disk, or emission or scattering from a wind. Such irradiation will be most important for relatively cool zones of the disk (Hubeny 1990b), for which the contrast between the color temperature of incident radiation and the photospheric gas temperature is largest. Since the far- and mid-UV spectra of disks are dominated by the inner disk, it is reasonable as a first step to neglect this complication, provided that the disk is viewed as a whole. If spectra from isolated portions of the disk are considered, irradiation becomes a larger issue, even in the UV.

Finally, within the class of hydrostatic, non-irradiated models there are some important questions to be further explored, concerning, e.g., line blanketing, or non-LTE treatment of stratification and radiative transfer. These issues are common to all computations of astrophysical atmospheres, whether stars or disks. The model spectra presented here serve as a reference, against which to compare spectra computed under different assumptions or approximations.

6. SUMMARY

Based on the need for detailed models to compare with modern observations of disks in CVs, we have presented a grid of far- and mid-UV spectra of steady-state, hydrostatic, non-irradiated accretion

disks. The grid covers a significant range of M_{wd} and \dot{m} , suitable for comparison with novalike variables or dwarf novae in outburst. The grid consists of 26 model disks, with spectra computed for each of them at six inclination angles. The models were computed using computer programs TLUSDISK, SYN-SPEC, and DISKSYN. A basic set of continuum opacities was used in the calculation of vertical stratification, but a large line list was used in the computation of the emergent spectra. The emergent spectra take account of limb darkening, and also of Doppler shifts due to orbital motion of the gas in the disk around the central white dwarf. Occultation of part of the inner disk by the central star is also taken into account.

The spectra extend from 850 Å to 2000 Å, suitable for comparison with *IUE*, *HST*, *HUT*, *ORFEUS*, and *FUSE* spectra. The models extend to cool enough temperatures that essentially all of the light produced by the disk at the wavelengths of interest is accounted for. Machine-readable files accessible via *anonymous ftp* provide tabulations of the spectra at 0.25 Å steps with a FWHM resolution of 1.0 Å. The spectra are presented in the form of *non-projected* fluxes for a disk viewed from a distance of 100 pc. For comparison with observations, the disk fluxes may need to be supplemented with fluxes from the appropriately occulted central star.

The radiative properties of both individual annuli and full disks are discussed with illustrative examples, to show how the disk spectra incorporate information about projected gas velocities and the variation of T_{eff} with radial distance from the white dwarf. In the disks considered, which are optically thick at all radii, the local UV spectra resemble spectra of stars that share the same T_{eff} and $\log g$. Fluxes and colors (flux ratios) of the integrated disk spectra depend on M_{wd} and \dot{m} . Limb darkening is shown to have a strong effect in the ultraviolet, affecting both the overall flux level and colors of the disk. Line broadening and blending is complex and non-intuitive in these disks. Synthetic spectra such as those presented here may be needed to understand the details of observed spectra, or even in some cases to identify the lines responsible for a given spectral feature. Despite trends in the disk spectra that are evident with varying accretion rate or inclination, spectra from rather different models may nevertheless appear quite similar, and additional information about the CV may be required to decide on a unique, best model.

Several possible improvements or additions to the

present set of models are discussed. As such models become available it will be of interest to compare the resulting spectra with those presented here. In the meantime, the present grid of spectra represents a self-consistent treatment of both the vertical stratification and emergent spectral properties of steady-state disks, with sufficient detail in the computation of the line spectrum to be of use in analyzing observed spectra of CV disks.

Support from NASA grants NAG5-1698, NAG5-2125, NAGW-3171, and NAG5-3459 is gratefully acknowledged.

REFERENCES

- Diaz, M. P., Wade, R. A., & Hubeny, I. 1996, *ApJ*, 459, 236
- Herter, T., Lacasse, M. G., Wesemael, F., & Winget, D. E. 1979, *ApJS*, 39, 513
- Hubeny, I. 1988, *Comp. Phys. Commun.*, 52, 103
- Hubeny, I. 1990a, *ApJ*, 351, 632
- Hubeny, I. 1990b, in *IAU Colloquium 129, Structure and Emission Properties of Accretion Disks*, ed. C. Bertout et al. (Gif sur Yvette: Editions Frontieres), 227
- Hubeny, I., Lanz, T., & Jeffery, C. S. 1994, *St. Andrews Univ. Newsletter on Analysis of Astronomical Spectra*, 20, 30
- Knigge, C., Long, K. S., Blair, W. P., & Wade, R. A. 1997, *ApJ*, 476, 291
- Knigge, C., Long, K. S., Wade, R. A., Baptista, R., Horne, K., Hubeny, I., & Rutten, R. G. M. 1998, *ApJ*, 499, 414
- Kříž, S., & Hubeny, I. 1986, *Bull. Astron. Inst. Czechosl.*, 37, 129
- Kurucz, R. L. 1979, *ApJS*, 40, 1
- Kurucz, R. L. 1991, *Stellar Atmospheres: Beyond Classical Models*, ed. L. Crivellari et al. (Dordrecht: Kluwer), 441
- Kurucz, R. L. 1994, *Kurucz CD-ROM No. 19* (Cambridge, MA: SAO)
- Kurucz, R. L. & Bell, B. 1995, *Kurucz CD-ROM No. 23* (Cambridge, MA: SAO)
- la Dous, C. 1989, *A&A*, 211, 131
- la Dous, C. 1994, *Space Science Rev.*, 67, 1

Long, K. S., Wade, R. A., Blair, W. P., Davidsen, A. F., & Hubeny, I. 1994, *ApJ*, 426, 704

Lynden-Bell, D., & Pringle, J. E. 1974, *MNRAS*, 168, 603

Nauenberg, M. 1972, *ApJ*, 175, 417

Nguyen, Q., Fabian, D., Belle, K., Huang, M., & Sion, E.M. 1998, *PASP*, 110, 39

Pereyra, N.A., Kallman, T.R., & Blondin, J.M. 1997, *ApJ*, 477, 832

Polidan, R. S., Mauche, C. W., & Wade, R. A. 1990, *ApJ*, 356, 211

Pringle, J. E. 1981, *ARA&A*, 19, 137

Proga, D., Stone, J. M., & Drew, J. E. 1998, *MNRAS*, 295, 595

Robinson, E. L., et al. 1995, *ApJ*, 443, 295

Robinson, E. L, Wood, J. H., & Wade, R. A. 1998, in preparation.

Shaviv, G., & Wehrse, R. 1986, *A&A*, 24, 337

Wade, R. A. 1984, *MNRAS*, 208, 381

Wade, R. A. 1991, in *Extreme Ultraviolet Astronomy*, ed. R. F. Malina & S. Bowyer ((New York: Pergamon Press), 186

Wade, R. A. 1996, in *Cataclysmic Variables and Related Objects*, ed. A. Evans & J. H. Wood (Dordrecht: Kluwer), 123

Williams, R. E., & Ferguson, D. H. 1982, *ApJ*, 257, 672

Fig. 1.— Rest-frame spectra (surface Eddington flux H_λ) for three rings of disk model *jj*. These rings, Numbers 18, 22, and 26, have $T_{\text{eff}} = 29150$ K, 19650 K, and 13140 K respectively. Left panel: spectra are shown at full computed resolution, maximum stepsize = 0.02 Å. Right panel: spectra are shown after convolution with a Gaussian instrumental profile, FWHM = 0.2 Å. Different spectral features form at different characteristic temperatures.

Fig. 2.— Non-projected far-UV fluxes from disk model *bb*, viewed at 100 pc distance. The disk is viewed nearly face-on. Three instrumental resolutions are shown, specified by Gaussian FWHM = 0.1, 1.0, and 3.5 Å. FWHM = 3.5 Å roughly corresponds to the resolution of the *HUT*, while *FUSE* is expected to resolve better than 0.1 Å. The disk models do not include wind lines.

Fig. 3.— Non-projected flux f_ν , averaged over the band 1450 — 1460 Å, in mJy. (One milliJansky = 10^{-26} erg cm $^{-2}$ s $^{-1}$ Hz $^{-1}$). The fluxes refer to disks viewed at a distance of 100 pc. Limb darkening and line blending appropriate to $\mu = \cos i = 0.750$ have been taken into account. Points corresponding to disk models *d*, *m*, *x*, *ff*, and *jj* are labeled. Solid lines connect models with the same M_{wd} (rightmost curve 0.35 M_\odot , leftmost curve 1.21 M_\odot). Dashed lines connect models with roughly the same T_{max} (lowest curve $\sim 16,500$ K, uppermost curve $\sim 92,000$ K).

Fig. 4.— Ratios of flux f_ν , for disks viewed from an inclination $i = 41.4^\circ$ ($\mu = 0.750$). Points corresponding to disk models *d*, *m*, *x*, and *ff* are labeled. Solid lines connect models with the same M_{wd} (rightmost curve 0.35 M_\odot , leftmost curve 1.21 M_\odot). Dashed lines connect models with roughly the same T_{max} (lowest curve $\sim 16,500$ K, uppermost curve $\sim 92,000$ K. The color range (at a fixed value of μ) is narrower for the flux ratio involving longer wavelengths, as expected.

Fig. 5.— Solid circles: the non-projected fluxes f_ν at 1075, 1455, and 1945 Å (top to bottom, at $\mu = 1$) for disk model *bb* ($M_{\text{wd}} = 0.550 M_\odot$, $\dot{m} = 10^{-8.5} M_\odot \text{ yr}^{-1}$). Open circles: the same for disk model *z* ($M_{\text{wd}} = 1.210 M_\odot$, $\dot{m} = 10^{-9.0} M_\odot \text{ yr}^{-1}$). Model *bb* has $T_{\text{max}} = 39110$ K, while model *z* has $T_{\text{max}} = 51520$ K. Colors (flux ratios) and fluxes clearly depend on μ , in addition to M_{wd} and \dot{m} . Non-projected flux shows the effect of limb darkening.

This 2-column preprint was prepared with the AAS L^AT_EX macros v4.0.

ing only; multiply by a factor $\mu = \cos i$ to account for geometric foreshortening. One milliJansky (mJy) = 10^{-26} erg cm $^{-2}$ s $^{-1}$ Hz $^{-1}$.

Fig. 6.— Far-UV fluxes f_λ , normalized at 1330 Å, for a sequence of disk models (m , n , p , q , cc , hh) with constant white dwarf mass but increasing \dot{m} (bottom to top). All spectra are shown as seen from a viewing direction $i = 60^\circ$ ($\mu = \cos i = 0.50$). Spectra are convolved with a Gaussian instrumental profile, FWHM = 1.0 Å.

Fig. 7.— Mid-UV fluxes f_λ , normalized at 1950 Å, for the same sequence of disk models shown in Fig. 6. Details are the same as for Figure 6.

Fig. 8.— Far-UV, non-projected fluxes f_λ from disk model bb , ($M_{\text{wd}} = 0.550 M_\odot$, $\dot{m} = 10^{-8.5} M_\odot \text{ yr}^{-1}$), for six inclinations, $\mu = 0.99, 0.95, 0.75, 0.50, 0.25$, and 0.15 (top to bottom). The $\mu = 0.99$ curve is offset vertically by 0.5×10^{-11} erg cm $^{-2}$ s $^{-1}$ Å $^{-1}$ and shown with a heavier line for clarity. Effects of limb darkening and line blending are apparent. Fluxes should be multiplied by a factor $\mu = \cos i$ to account for geometrical foreshortening.

Fig. 9.— Details of the mid-UV spectra of a sequence of disk models, showing the characteristic features of disks as a function of disk temperature T_{max} . The spectra are shown as seen from a viewing angle of $i = 8.1^\circ$ so that line blending is minimized. Non-projected fluxes are for a viewing distance of 100 pc. As with all figures in this report, the flux from the white dwarf is not included.

Fig. 10.— A comparison of two closely matched disk spectra. Each model disk (v , cc) has the same run of T_{eff} with dimensionless radius x , and the viewing angles $\mu = \cos i$ have been chosen to match approximately the run of projected velocities $v(x) \sin i$. Finally, the fluxes have been normalized at 1950 Å (upper panel) or 1330 Å (lower panel). The spectrum of model v is plotted with a heavier line for clarity. Residual differences between the spectra are due to limb darkening and a systematic difference in effective gravities amounting to about 0.17 dex (see Table 2).

TABLE 1
ADOPTED WHITE DWARF PARAMETERS

M_{wd} (M_{\odot})	R_{wd} (10^9 cm)	$\log g$	v_{surf} (km s $^{-1}$)	M_{wd}/R_{wd}^3 ^a
0.35	1.142	7.55	2020	0.2374
0.55	0.905	7.95	2840	0.7423
0.80	0.699	8.34	3890	2.347
1.03	0.518	8.71	5140	7.423
1.21	0.378	9.05	6520	22.35

^aUnits are $M_{\odot}/(10^9 \text{ cm})^3$.

TABLE 2
PARAMETERS OF DISK MODELS

(EXTERNAL PLANOTABLE, PORTRAIT MODE)

TABLE 3
TEMPERATURE STRUCTURE OF SELECTED DISK MODELS

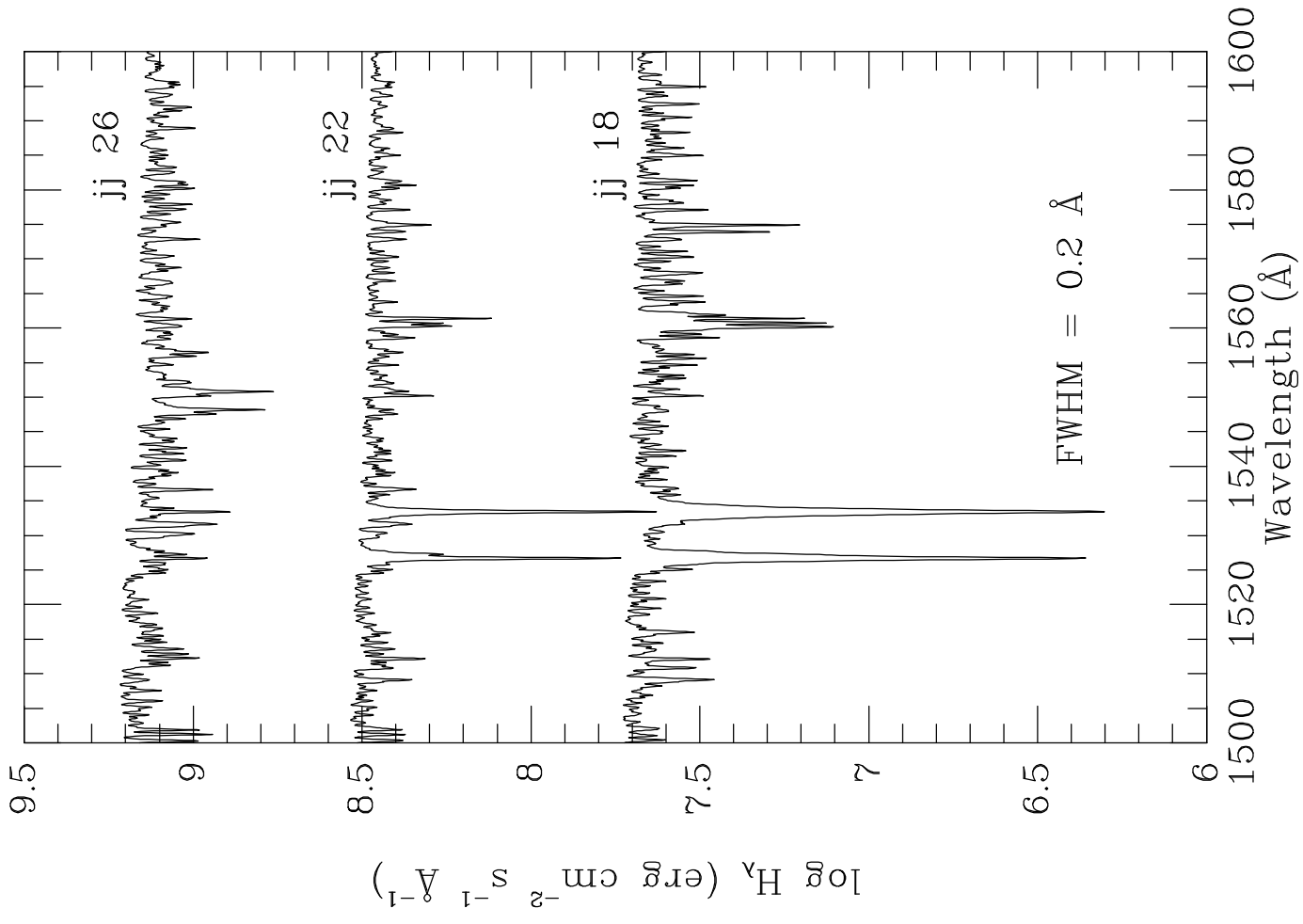
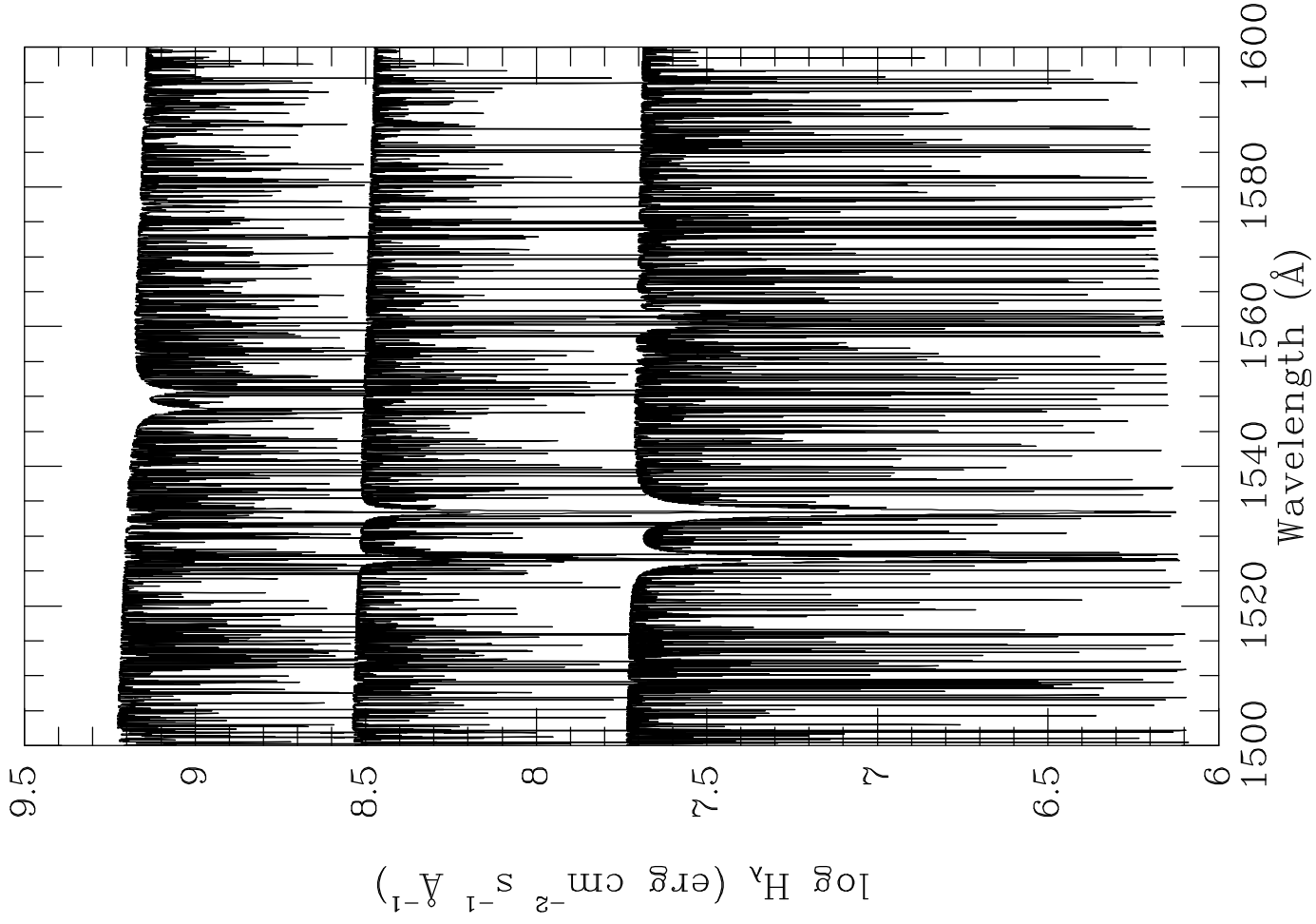
(EXTERNAL PLANOTABLE, LANDSCAPE MODE)

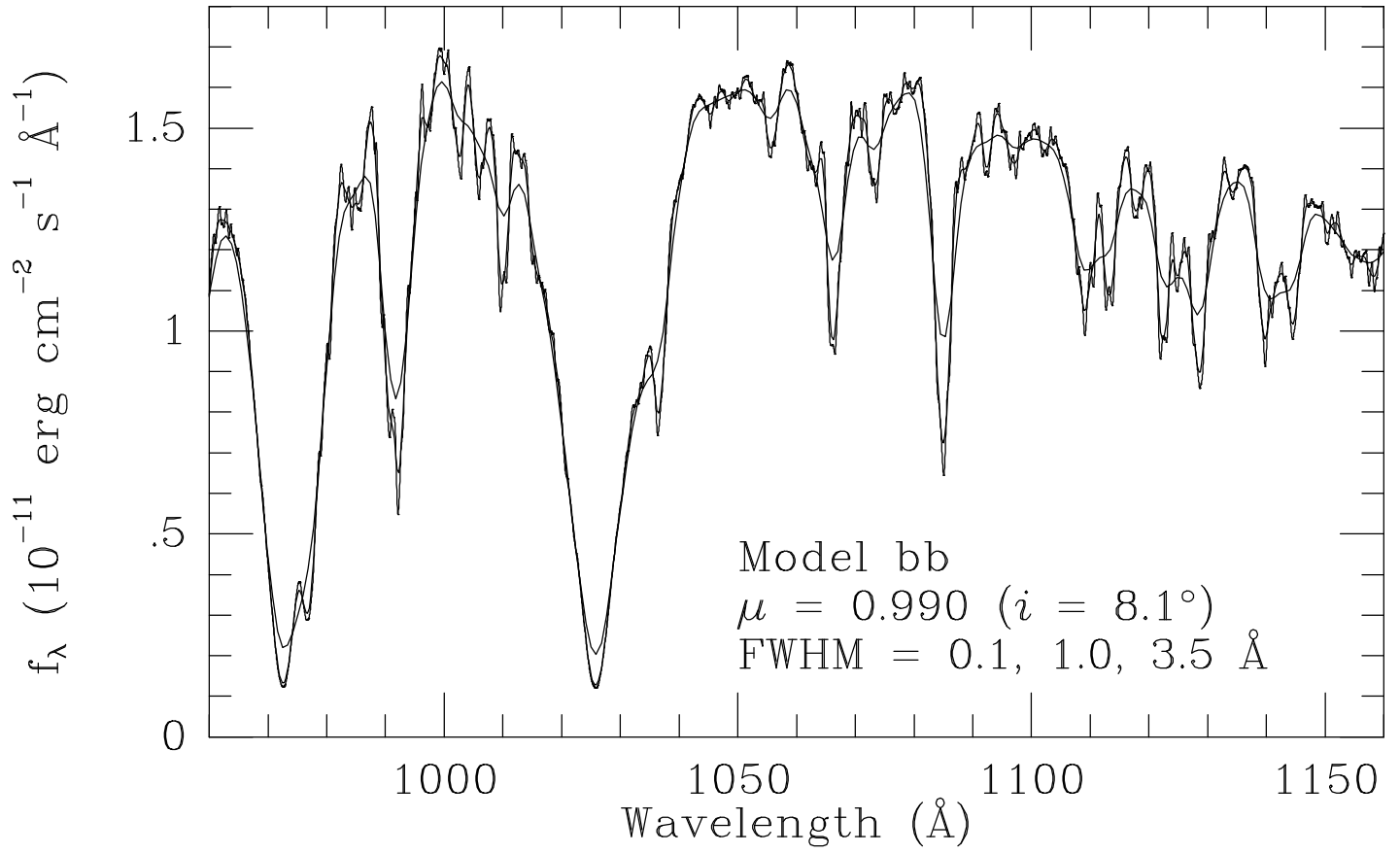
TABLE 4
INCLINATION ANGLES FOR COMPUTED DISK SPECTRA

$\mu = \cos i$	i	$\sin i$
0.990	8°:1	0.141
0.950	18°:2	0.312
0.750	41°:4	0.661
0.500	60°:0	0.866
0.250	75°:5	0.968
0.150	81°:4	0.989

TABLE 5
SAMPLE TABLE FOR MODEL ZZ

(EXTERNAL PLANOTABLE, LANDSCAPE MODE)





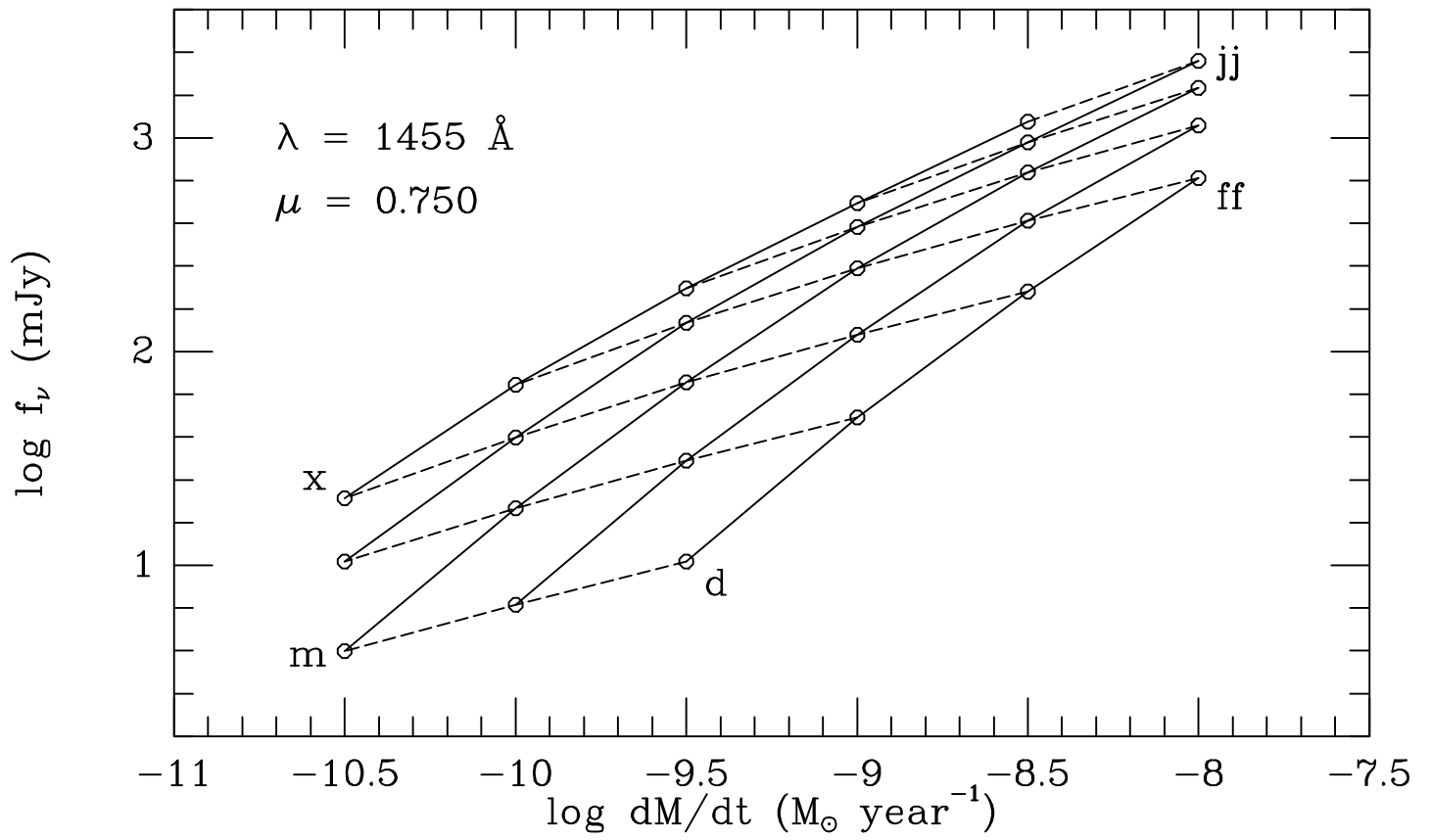
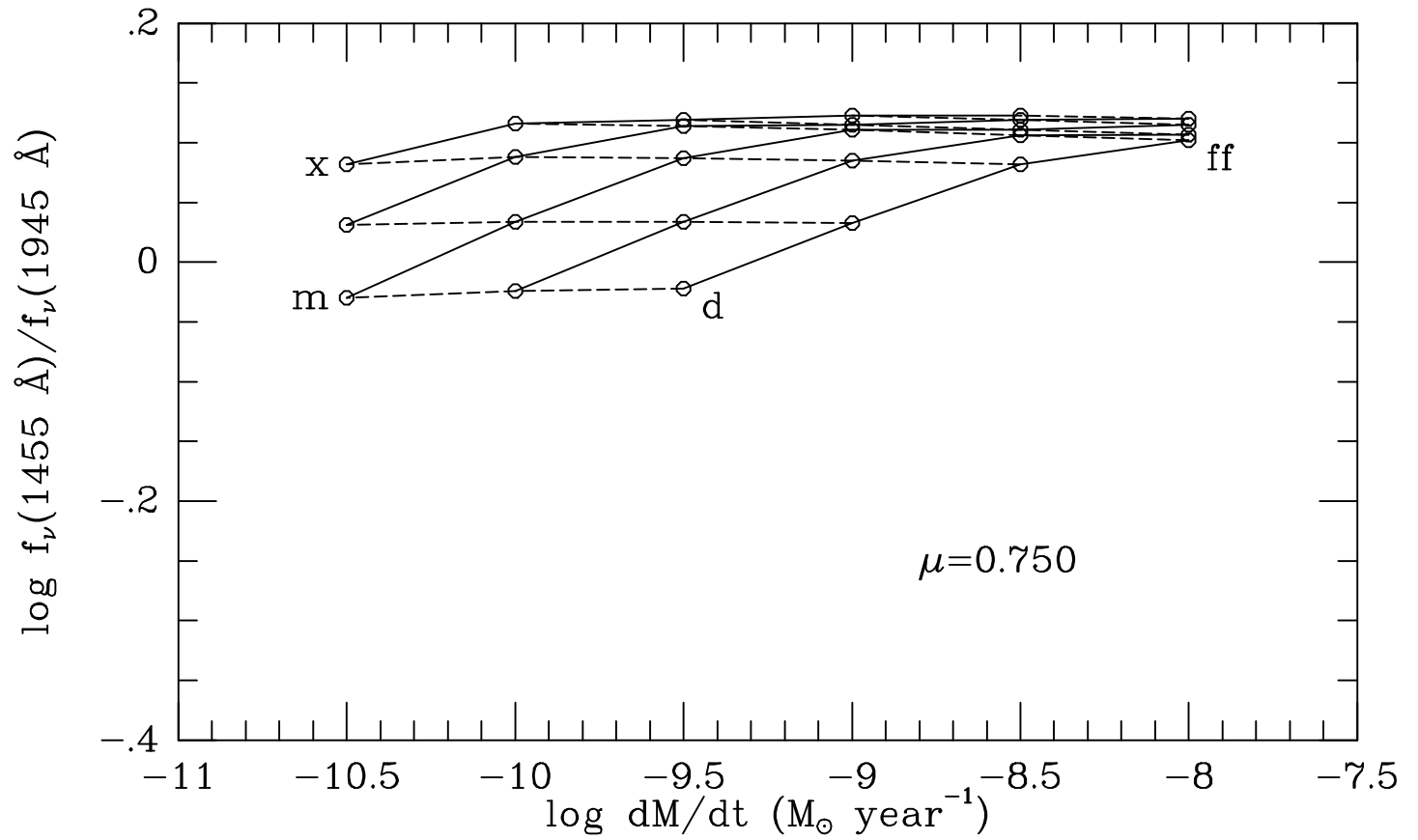
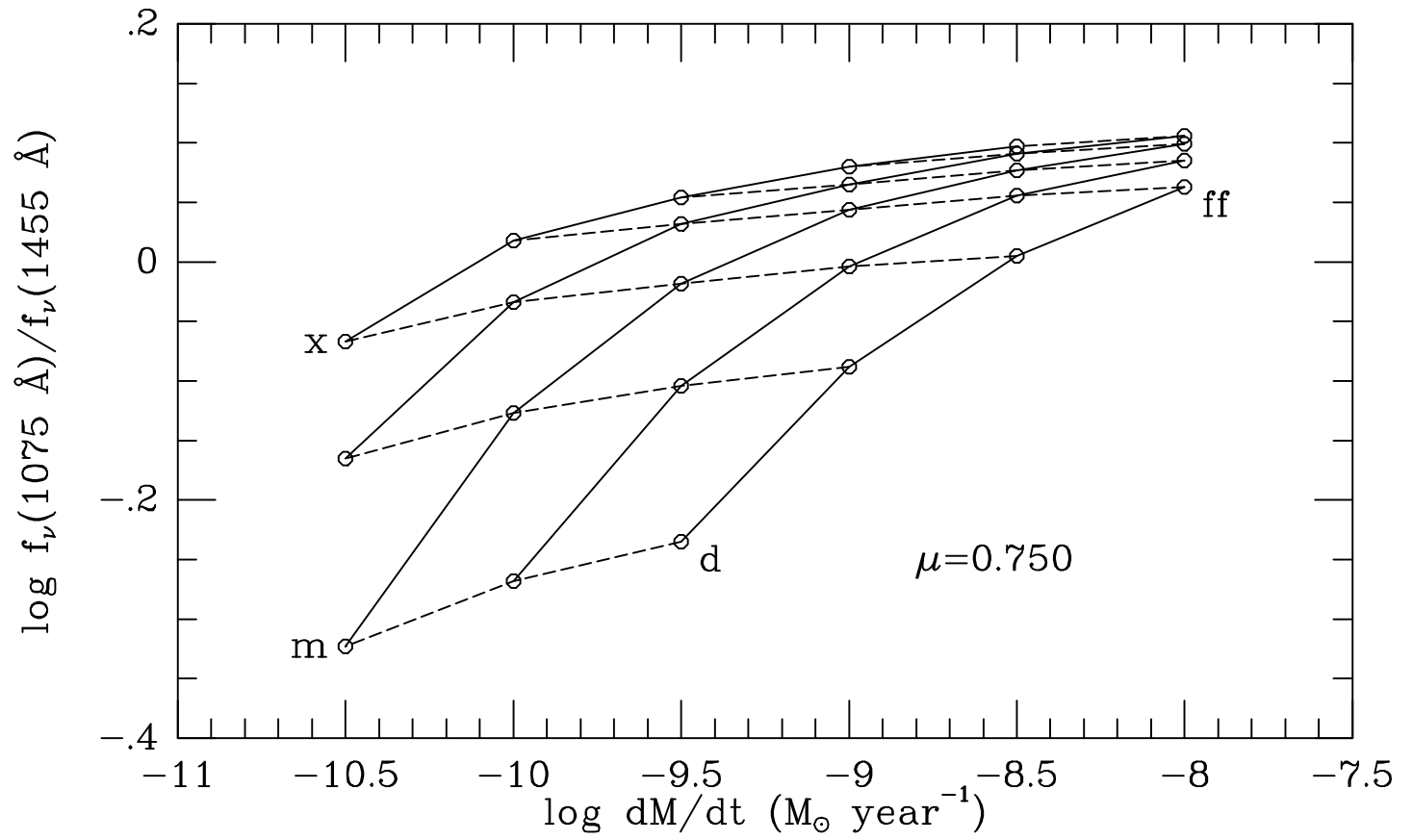


TABLE 3
TEMPERATURE STRUCTURE OF SELECTED DISK MODELS

Ring	$x = r/R_{wd}$	Model m T_{eff}	Model n T_{eff}	Model p T_{eff}	Model q T_{eff}	Model cc T_{eff}	Model hh T_{eff}	Model jj T_{eff}
01	1.05	12840	17130	22840	30450	40610	54160	72220
02	1.20	16020	21360	28490	38000	50660	67560	90090
03	1.36	16490	22000	29330	39110	52160	69560	92760
04	1.56	16180	21580	28780	38380	51180	68250	91010
05	1.80	15450	20610	27480	36650	48870	65170	86910
06	2.05	14620	19500	26010	34680	46240	61670	82240
07	2.35	13680	18240	24320	32440	43250	57680	76920
08	2.70	12700	16930	22580	30110	40150	53450	71400
09	3.10	11730	15650	20860	27820	37100	49480	65980
10	3.55	10819	14430	19240	25660	34210	45630	60840
11	4.10	9900	13200	17600	23470	31300	41740	55660
12	4.70	...	12100	16140	21520	28690	38270	51030
13	5.40	...	11060	14750	19660	26220	34970	46630
14	6.20	...	10090	13460	17950	23930	31910	42560
15	7.10	12290	16390	21850	29140	38860
16	8.20	11140	14860	19820	26430	35240
17	9.40	10140	13530	18040	24060	32090
18	10.80	12290	16390	21860	29150
19	12.40	11160	14880	19850	26470
20	14.30	10100	13460	17960	23940
21	16.40	12220	16300	21730
22	18.90	11050	14730	19650
23	21.70	10010	13350	17800
24	25.00	12060	16080
25	28.80	10890	14530
26	33.10	13140
27	38.00	11880
28	43.70	10740



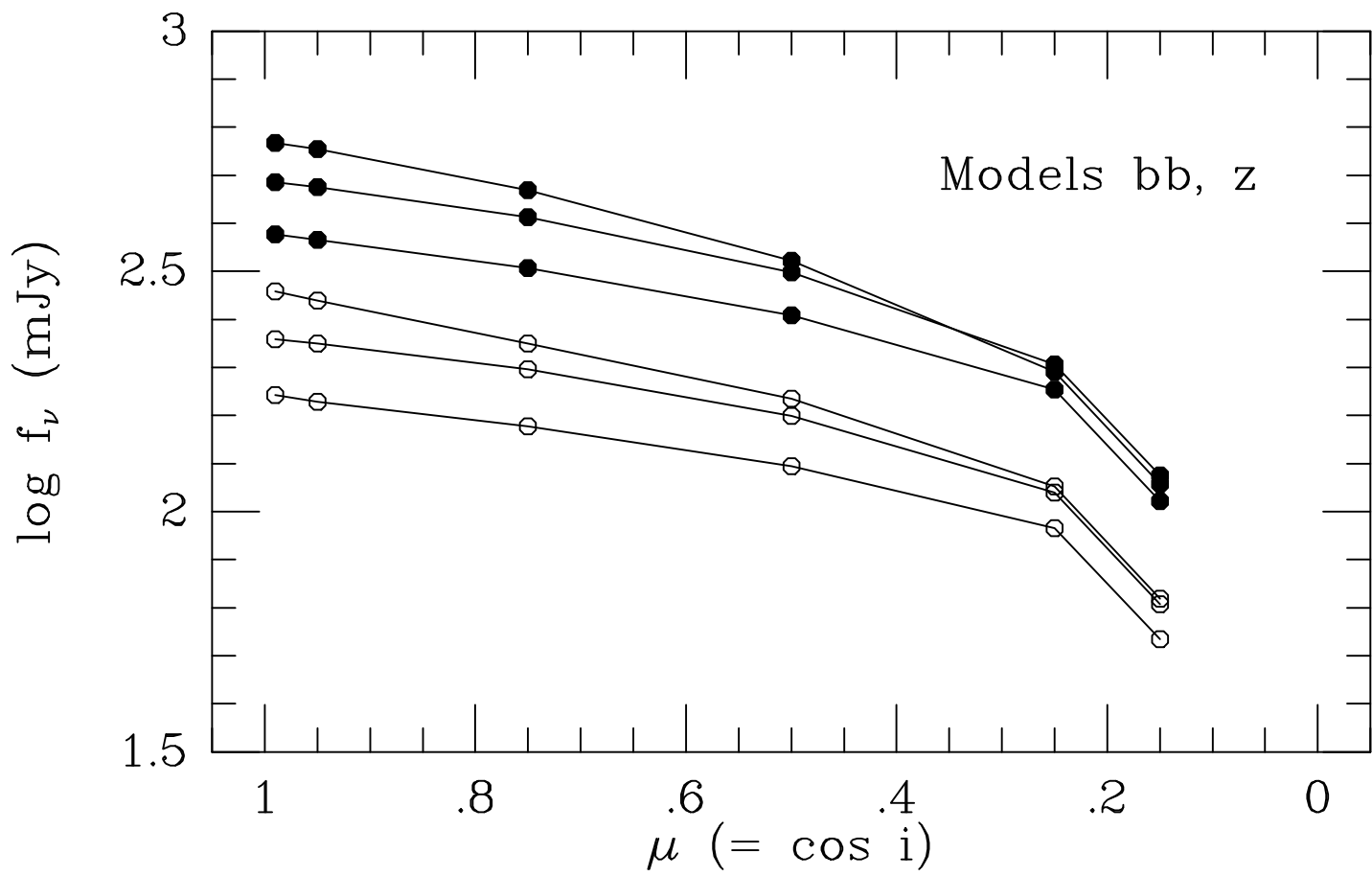
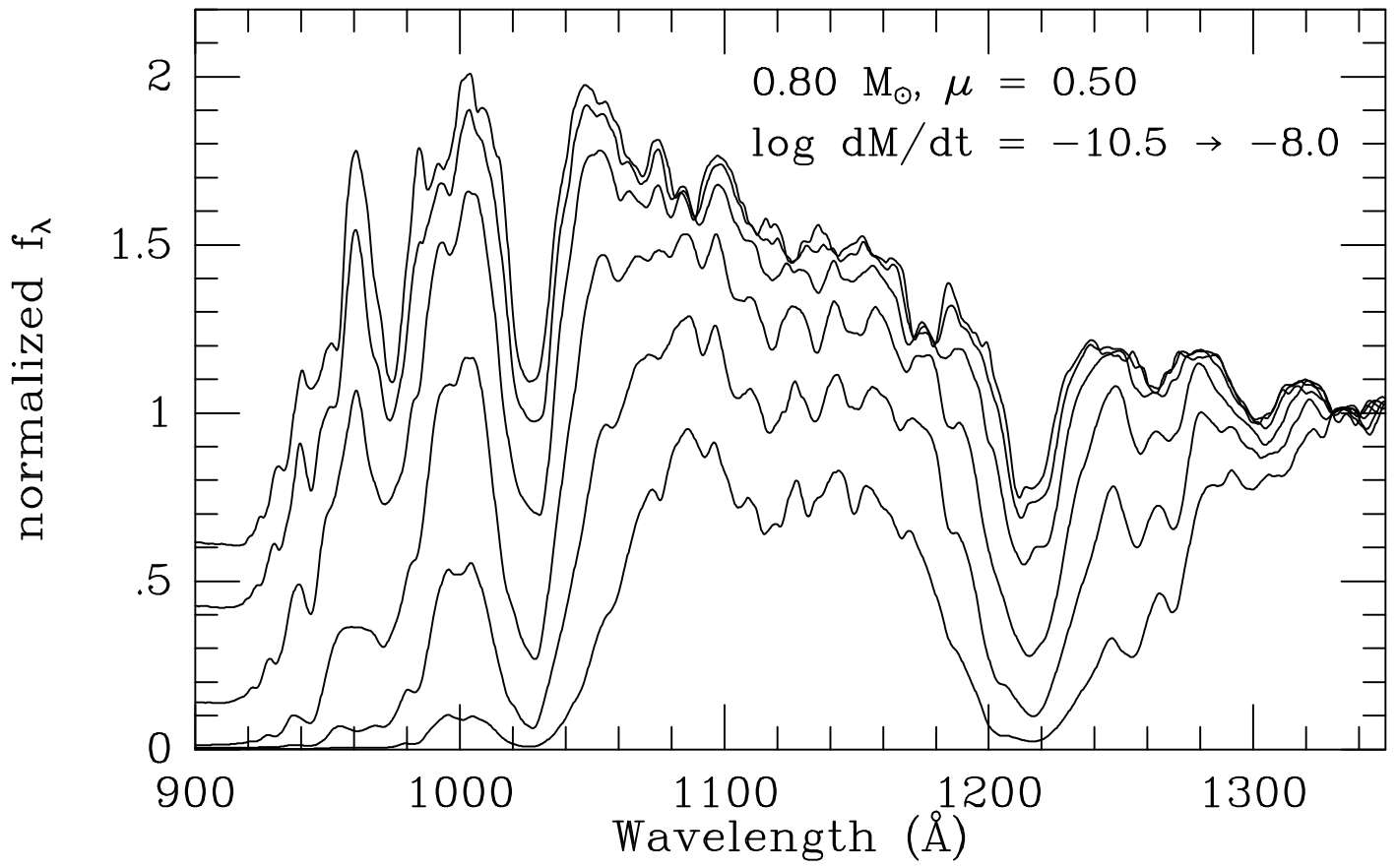
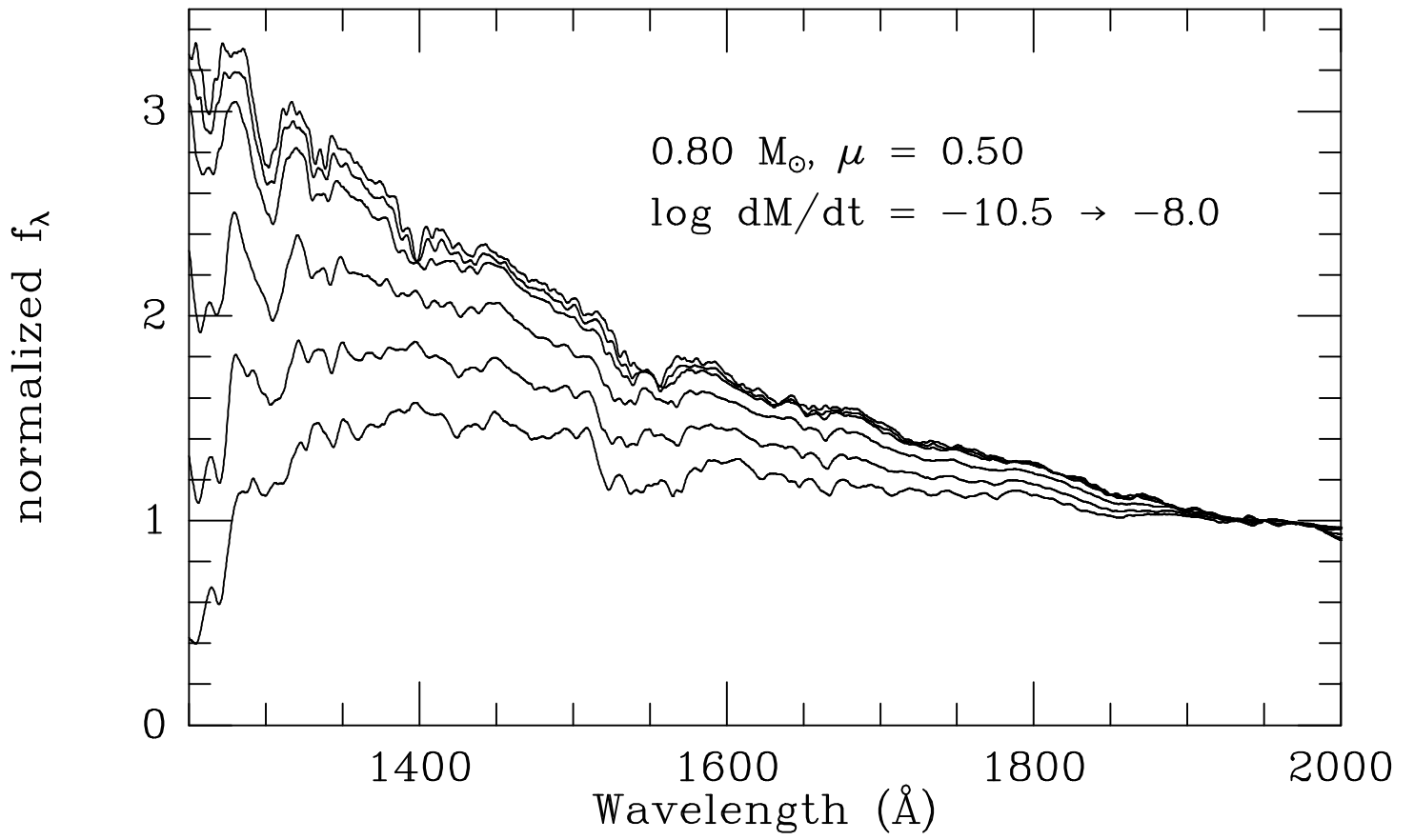
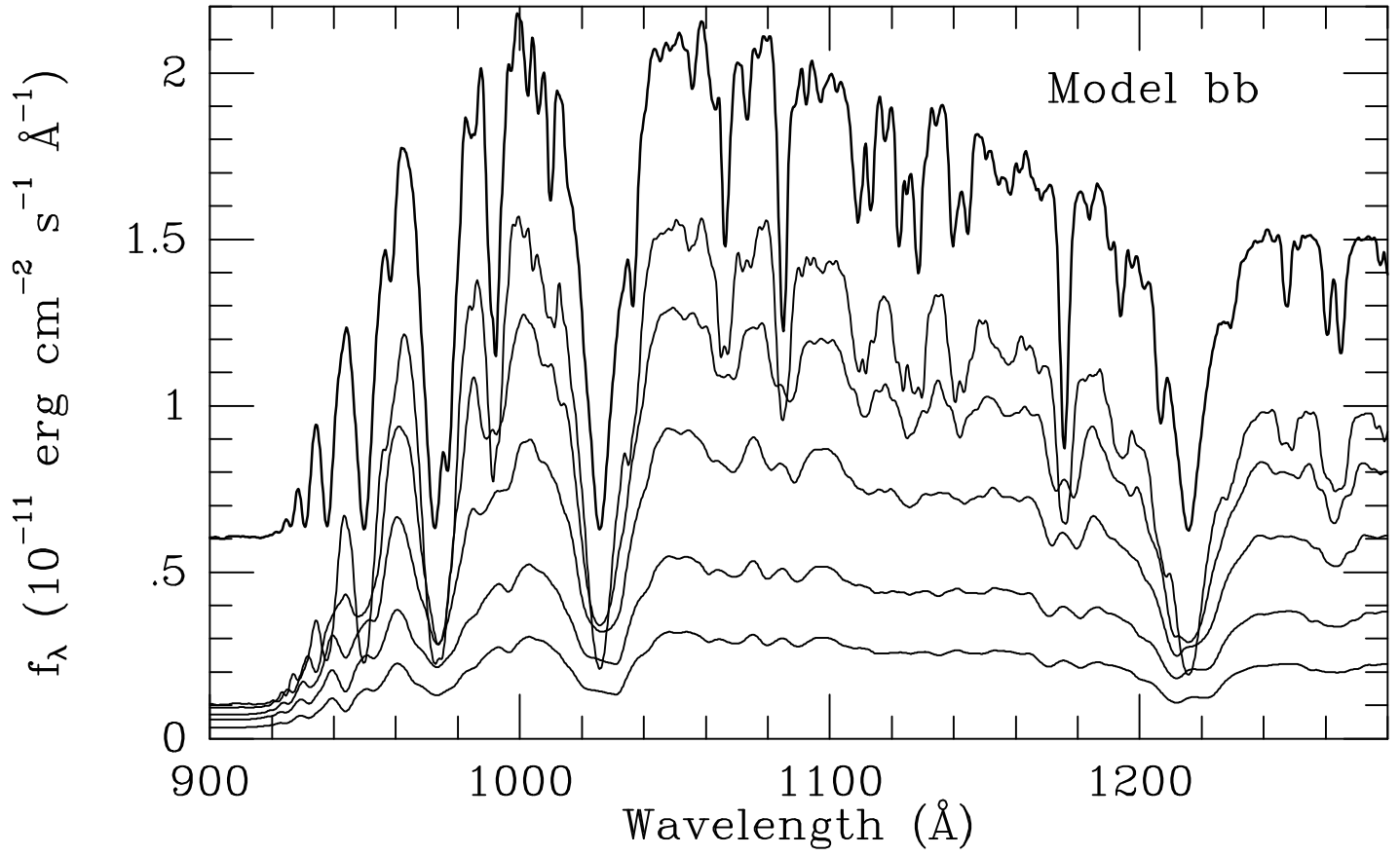


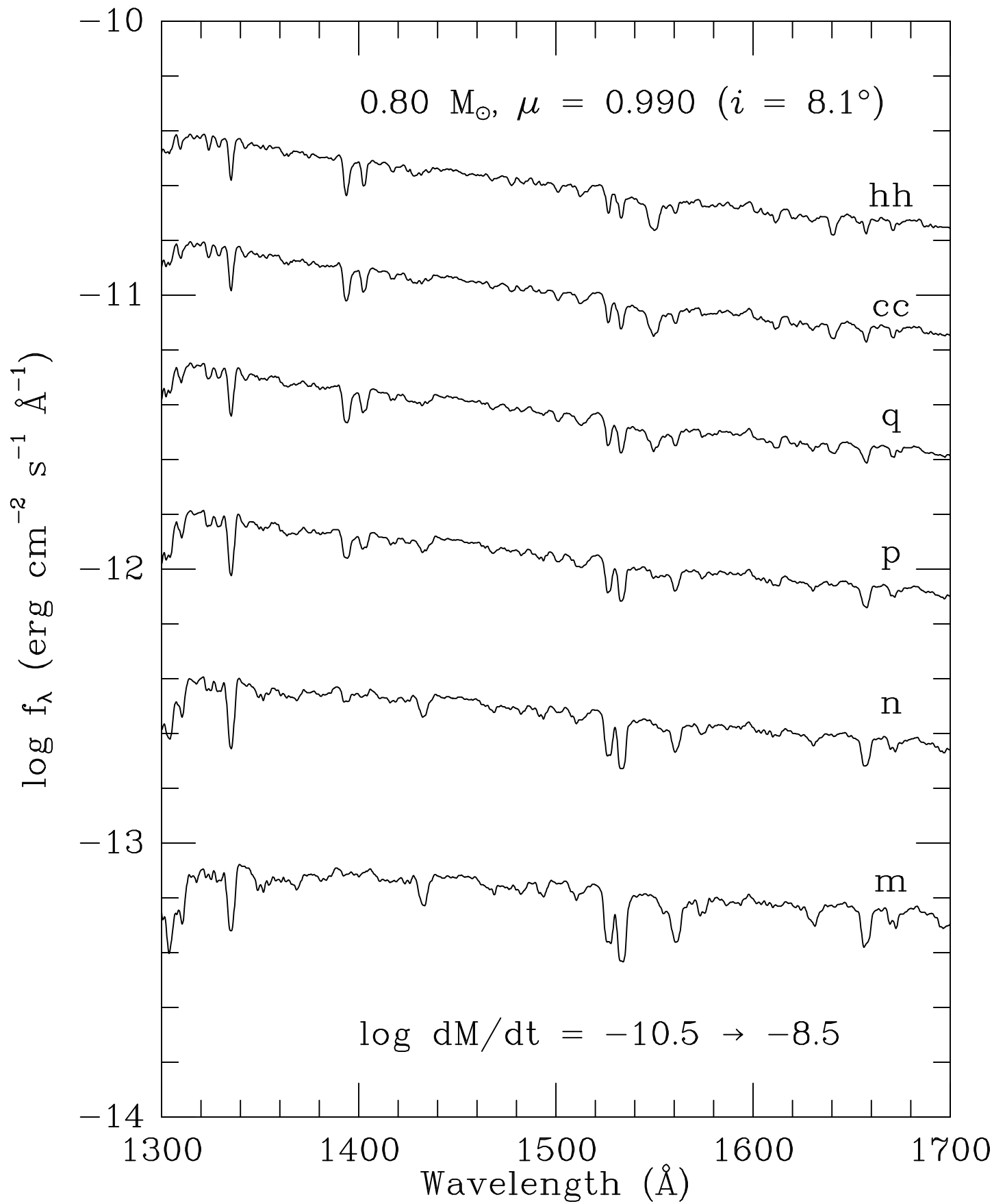
TABLE 5
EXCERPT FROM ASCII TABLE `zz.table` FOR MODEL `zz`

wavelength	mu=0.150	mu=0.250	mu=0.500	mu=0.750	mu=0.950	mu=0.990
850.000	2.21100E-12	3.78900E-12	4.68300E-12	5.39800E-12	5.84900E-12	5.91300E-12
850.250	2.21100E-12	3.78700E-12	4.68100E-12	5.39600E-12	5.84600E-12	5.90100E-12
850.500	2.21000E-12	3.78500E-12	4.67800E-12	5.39300E-12	5.84200E-12	5.88700E-12
850.750	2.20900E-12	3.78300E-12	4.67500E-12	5.38900E-12	5.83600E-12	5.87500E-12
851.000	2.20800E-12	3.78100E-12	4.67200E-12	5.38500E-12	5.82900E-12	5.86800E-12
851.250	2.20700E-12	3.78000E-12	4.67000E-12	5.38200E-12	5.82100E-12	5.86500E-12
...
1998.750	1.06600E-12	1.81100E-12	2.33700E-12	2.74100E-12	3.00400E-12	3.05800E-12
1999.000	1.06600E-12	1.81000E-12	2.33700E-12	2.74100E-12	3.00800E-12	3.06400E-12
1999.250	1.06600E-12	1.81000E-12	2.33600E-12	2.74000E-12	3.01200E-12	3.06700E-12
1999.500	1.06500E-12	1.80900E-12	2.33500E-12	2.74000E-12	3.01600E-12	3.06900E-12
1999.750	1.06500E-12	1.80900E-12	2.33400E-12	2.73900E-12	3.01900E-12	3.06900E-12
2000.000	1.06400E-12	1.80900E-12	2.33300E-12	2.73900E-12	3.02100E-12	3.06800E-12









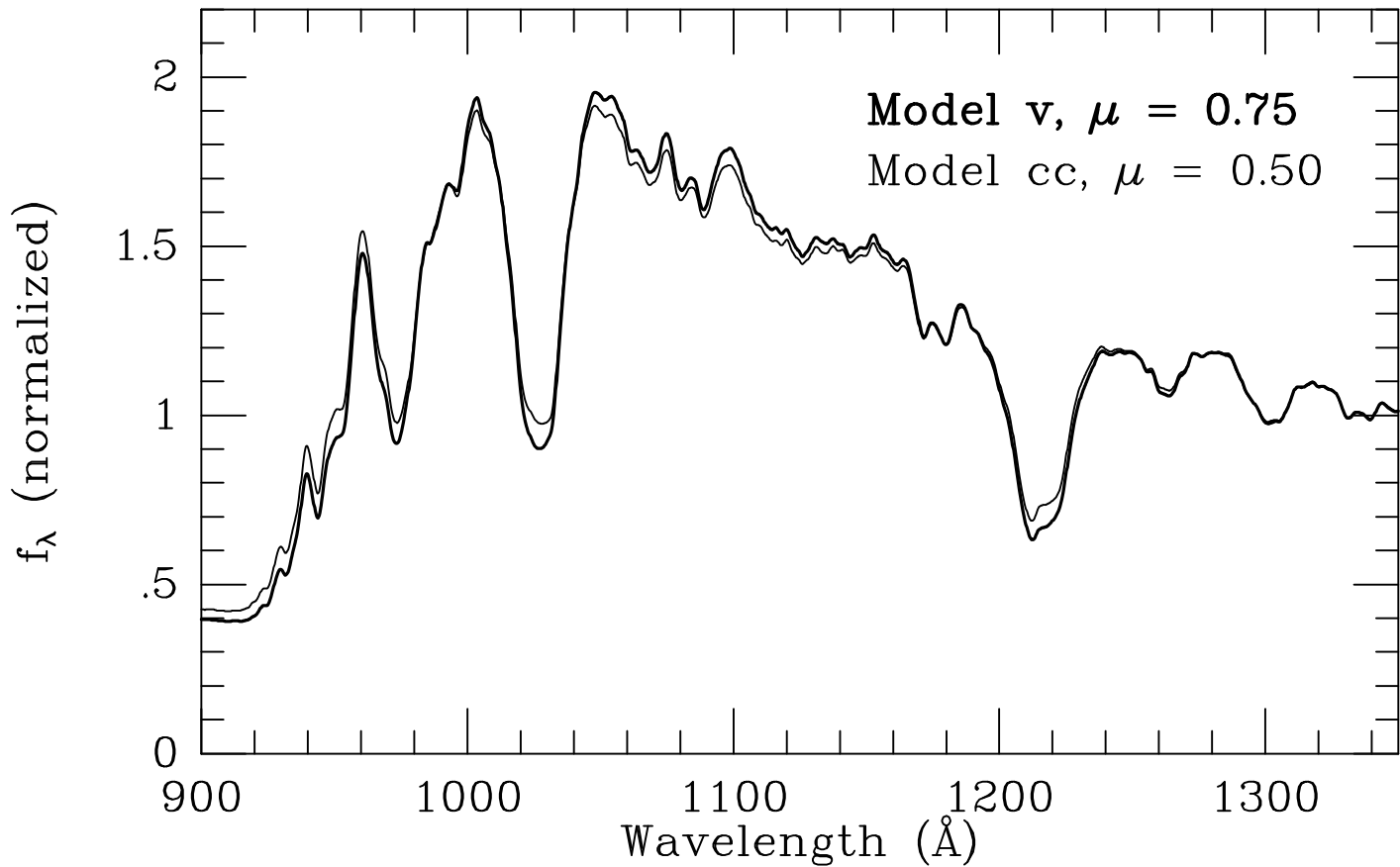
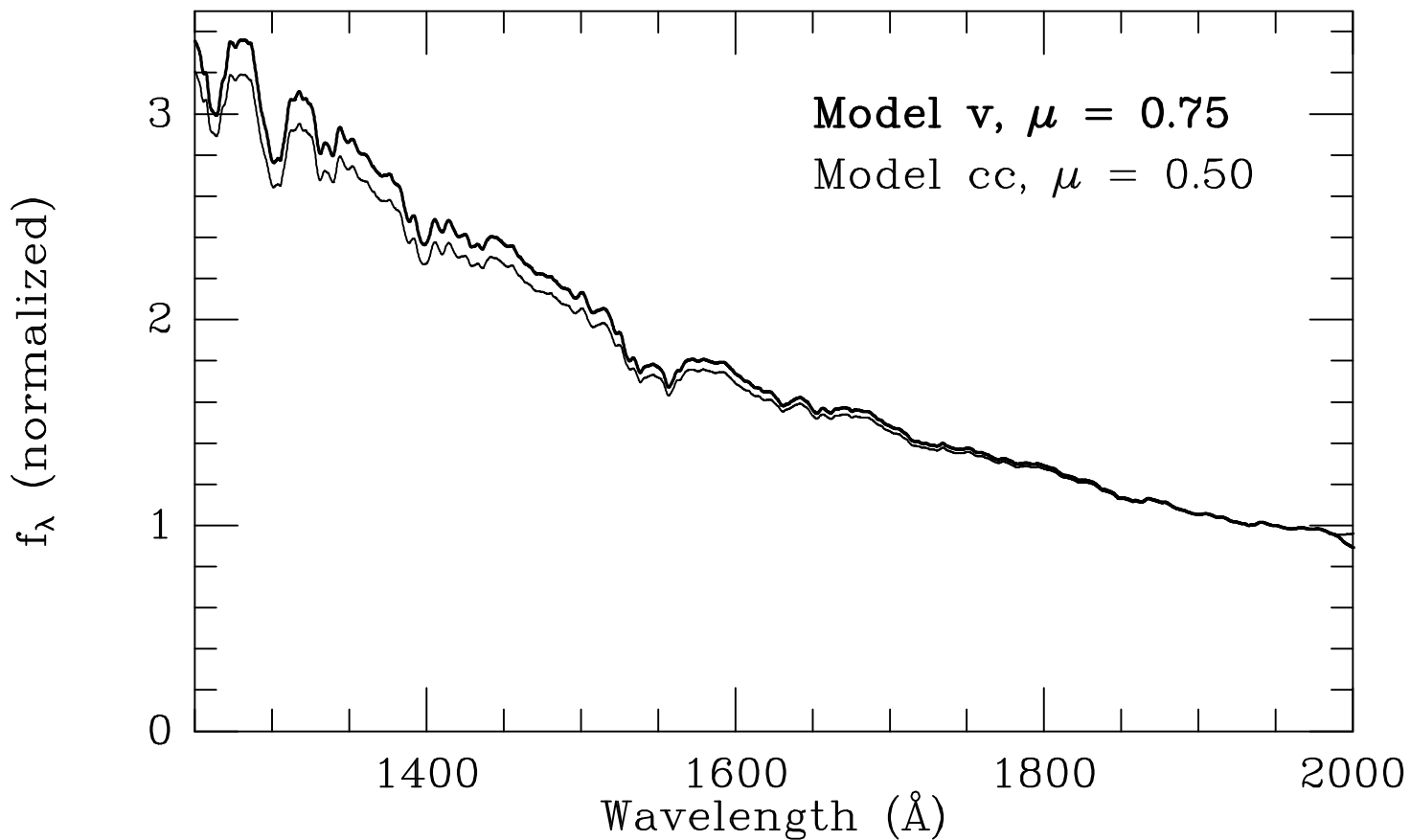


TABLE 2
PARAMETERS OF DISK MODELS

Name	M_{wd} (M_{\odot})	$\log \dot{m}$ ($M_{\odot} \text{ yr}^{-1}$)	Rings	T_{max} ^a	τ_c ^b	$\log g$ ^c	T_{out} ^d	$\log g$ ^e	$\log R_{out}$ (cm)
d	0.350	-9.5	1-11	16490	93	5.72	9900	4.86	9.67
e	0.350	-9.0	1-14	22000	200	5.85	10090	4.70	9.85
aa	0.350	-8.5	1-17	29330	216	5.98	10150	4.52	10.03
ff	0.350	-8.0	1-20	39110	520	6.09	10100	4.32	10.21
h	0.550	-10.0	1-11	16490	46	5.85	9900	4.95	9.57
j	0.550	-9.5	1-14	22000	76	6.00	10090	4.84	9.75
k	0.550	-9.0	1-17	29330	90	6.14	10150	4.67	9.93
bb	0.550	-8.5	1-20	39110	178	6.26	10100	4.47	10.11
gg	0.550	-8.0	1-23	52160	350	6.38	10100	4.27	10.29
m	0.800	-10.5	1-11	16490	8	5.95	9900	5.02	9.46
n	0.800	-10.0	1-14	22000	22	6.12	10090	4.95	9.64
p	0.800	-9.5	1-17	29330	41	6.29	10150	4.80	9.82
q	0.800	-9.0	1-20	39110	65	6.43	10100	4.62	10.000
cc	0.800	-8.5	1-23	52160	138	6.55	10100	4.43	10.18
hh	0.800	-8.0	1-25	69560	230	6.67	10890	4.36	10.30
s	1.030	-10.5	1-14	22000	7	6.21	10090	5.03	9.51
t	1.030	-10.0	1-17	29330	20	6.42	10150	4.92	9.69
u	1.030	-9.5	1-20	39110	28	6.59	10100	4.77	9.87
v	1.030	-9.0	1-23	52160	54	6.72	10100	4.58	10.05
dd	1.030	-8.5	1-25	69560	105	6.84	10890	4.53	10.17
jj	1.030	-8.0	1-28	92760	160	6.97	10740	4.31	10.36
x	1.210	-10.5	1-17	28970	7	6.48	10020	4.99	9.55
y	1.210	-10.0	1-20	38640	14	6.72	9970	4.86	9.73
z	1.210	-9.5	1-23	51520	22	6.88	9890	4.70	9.91
zz	1.210	-9.0	1-25	68710	48	7.00	10760	4.68	10.04
ee	1.210	-8.5	1-28	91620	79	7.13	10610	4.47	10.22

^aEffective temperature at $x = 1.36$.

^bMidplane Rosseland mean optical depth τ , at $x = 1.36$.

^c $\log g$ measured at $\tau = 1$, $x = 1.36$.

^dEffective temperature at the outermost ring.

^e $\log g$ measured at $\tau = 1$, outermost ring.